Analysis of JLab E12-14-012 Ti(e,e′ p) Data and Determination of the Ti Spectral Function

Clint A. Lanham

Dissertation submitted to the Faculty of the
Virginia Polytechnic Institute and State University
in partial fulfillment of the requirements for the degree of

Master of Science
in
Physics

Camillo Mariani, Chair
Thomas O'Donnell
Mark Pitt
Tatsu Takeuchi

May 26, 2023
Blacksburg, Virginia

Keywords: Argon, Cross Section, Isospin, Missing Energy-Momentum, Scattering, Spectral Function, Titanium

Analysis of JLab E12-14-012 Ti(e,e′ p) Data and Determination of the Ti Spectral Function

Clint A. Lanham

(ABSTRACT)

Future long baseline neutrino oscillation experiments like the Deep Underground Neutrino Experiment (DUNE) rely on Liquid Argon Time Projection Chamber (LArTPC) detectors. The reconstruction of neutrino flavors and energy through interactions with Argon is a critical issue for assuring the DUNE success. The neutrino-Argon nuclear cross section is one of the biggest sources of uncertainty in measuring possible Charge-Parity Violation (CPV) in the neutrino (ν) sector and decoupling background like matter-effects. This thesis summarizes the exclusive electron scattering measurement of the Jefferson Lab E12-14-012 experiment. The E12-14-012 experiment goals are to explore the Ti(e,e′p) and Ar(e,e′p) reactions in a wide range of kinematics in order to determine the spectral function of protons and neutrons in Argon. The measurements made in E12-14-012 are the first of their kind in argon and are a pivotal step in understanding the electron-Argon interaction and its relation to neutrino scattering. Titanium was specifically chosen under an assumption that its protons can be a proxy for argon neutron spectral functions. The analysis of the exclusive electron scattering in titanium is described in detail in this thesis.

Analysis of JLab E12-14-012 Ti(e,e′ p) Data and Determination of the Ti Spectral Function

Clint A. Lanham

(GENERAL AUDIENCE ABSTRACT)

While considerable progress has been made in understanding the power of the atom, nucleons (protons and neutrons) trapped in medium-to-heavy nuclei have properties that we still need to understand. The purpose of this thesis is to explore the nuclear investigation conducted at Jefferson Lab (JLab) in Newport News, Virginia. Specifically, we follow the data analysis of the JLab Hall A Experiment E12-14-012 which seeks to quantify the nuclear energy-momentum distributions of nucleons in complex nuclei like titanium and argon. These measurements, the first of their kind experimentally, are done to provide a reliable model for lepton-nucleus interactions. Modeling lepton-nucleus interactions in argon is of paramount importance, as argon is the primary target medium in future long baseline neutrino oscillation experiments like DUNE. Neutrinos are notoriously difficult to measure; and therefore, when they interact, we only measure the interaction products as they come out of the nucleus. Sometimes the products of the primary interaction will not escape the nucleus and have to be modelled to accurately estimate the incoming neutrino energy. The analysis on titanium provided in this thesis is a bridge for argon interactions with leptons, where titanium is used to determine argon neutron momentum and energy distributions.

Dedication

To the memory of a good friend and fellow Aggie

Daniel R. Partridge

(1991 - 2023)

"Here"

Acknowledgments

It takes a village to raise a child. This work is a lifetime of knowledge and philosophies funneled through me.

To Lane Buban who pushed my academic growth and introduced me to a wider world. To my first programming instructor, Jason Cordes, who stayed after-school to teach me and thereby supported my path to becoming a computational physicist. To Mike McCarley who taught me East Texas Math, a philosophy in and of itself, unlike any other. I can devote an entire dissertation to all of the many unnamed school teachers in my life. Their contribution has been truly invaluable.

To my very first college mentors, Dr. Casey Papovich and Dr. Vithal Tilvi. I cannot extol enough the patience they had as teachers. My appreciation for their words of wisdom has only increased as time has passed.

To every professor in the physics department at SHSU. Their dedication to mentoring students as their first and only priority is world-class.

To Dr. Joel Walker and Dr. James Dent for mentoring me through the MINER collaboration. Special thanks to Dr. Andy Kubik for being the lightning rod for my condensed matter questions. Further thanks to the MINER collaboration at-large for providing a valuable experience.

To my graduate mentors. Dr. Djordje Minic, who is a conduit of science and refreshing frankness. Dr. Travis Merritt, who has provided an invaluable service in revamping the lab curriculum, and I am grateful to have had the opportunity to help guide that vision with my fellow TAs in the trenches. Dr. Tatsu Takeuchi who always took the time to offer advice and kindness. Dr. C. Nadir Kaplan, who I had many insightful and friendly discussions

with. Dr. Wenya Shu, who has been extremely kind in teaching me a variety of numerical analysis concepts. Dr. Camillo Mariani, whose guidance and support cannot be overstated. To my graduate committee members overall for taking the time to oversee my growth.

To my friends and fellow graduates: Nabin Bhatta and Yulun Li. I could not have asked for two better roommates, aspiring chefs, or art critics. I will always cherish the memories we shared.

Thanks to my peers for an untold number of hours discussing, bemoaning, and accepting the life of a student.

To my family, the ones I did not have a say in and the ones I chose this past March. Without their support, I would never have made it here.

Last but not least, to my wife Pari Lanham. She had the mixed fortune of graduating before me, and has had the unenviable task of being married to a grad student. Her love and support make anything possible.

Contents

List of Figures

List of Tables

List of Abbreviations

E_{miss} Missing Energy

p_{miss} Missing Momentum

DUNE Deep Underground NEutrino Experiment

DWIA Distorted Wave Impulse Approximation

FD Far Detector

FSI Final State Interactions

m.w.e. Meter Water Equivalent

ND Near Detector

PMNS Pontecorvo-Maki-Nakagawa-Sakata matrix

PWIA Plane Wave Impulse Approximation

SIMC Symbolic Implicit Monte Carlo

SURF Sanford Underground Research Facility

Chapter 1

Introduction

The purpose of this thesis is to analyze the data collected in 2017 by the Jefferson Lab experiment E12-14-012. Jefferson Lab (JLab) is located in Newport News, Virginia. The JLab E12-14-012 experiment seeks to measure Ar(e,e′p) and Ti(e,e′p) exclusive cross sections and determine the spectral functions of protons and neutrons in the Argon nuclei.

This introductory chapter serves as an overview of the physical foundations and justification for the experiment. Chapter 2 touches on the experimental setup at JLab. Chapter 3 explains the data fitting process, using previous Ar(e,e′p) data analysis as a foil. Chapter 4 focuses on the Ti(e,e′p) data analysis through the inclusion of a co-authored paper. Chapter 5 is the conclusion and covers the final remarks.

1.1 Motivation

This experiment at JLab is meant to investigate many aspects of nuclear theory. This thesis will focus on the experiment's probe into the properties of protons and neutrons bound in argon (i.e., the position and width of the proton and neutron shells in argon). Argon nuclei are frequently used in particle detectors. Argon is a non-isotropic nuclei, and it is not well understood. The original proposal for the experiment highlighted the utility in understanding neutrino and anti-neutrino interactions in argon [1]. Neutrino and anti-neutrino interactions are identified by looking at the charged and neutral particles that are generated

when the neutrino or anti-neutrino interact on the detector target. The type of particles that are emitted and their energy-momentum depends on nuclear effects and ultimately on the nucleon-nucleon correlations inside nuclei. Understanding these properties would be essential for future neutrino studies like the Deep Underground Neutrino Experiment (DUNE), which will use liquid argon time projection chamber (LArTPC) detectors [1, 2].

DUNE is a major international collaboration centered around Fermilab and Sanford Lab [3]. Fig. 1.1 shows an overview of the DUNE facility setup, from right to left, the neutrino beam facility and the "near detector" (ND) complex, both hosted at Fermilab, and the "far detector" (FD) lab that will be deep underground (4,850-m.w.e.) at the Sanford Underground Research Facility (SURF). The Fermilab Long-Baseline Neutrino Facility accelerates a proton beam to 1 MW[1]. The neutrino and antineutrino will originate from the decay of pions and kaons produced by the proton beam interaction with a graphite target. Within the neutrino production line, DUNE selects positive/negative pions using a set of magnetic horns. The pions quickly decay into positive/negative muons and neutrinos/anti-neutrinos. At the end of the production line, shielding absorbs any muons. Neutrinos are left to proceed 304 m to the ND. Neutrinos and antineutrinos are produced with an energy spectrum between 1 and 8 GeV.

From the ND, the neutrinos travel 1,300-km through the Earth towards the FD that is located at SURF.

Utilizing this neutrino beam, DUNE has several ambitious scientific goals that focus on neutrino oscillation physics and tests of the standard model. The main DUNE focus is to measure leptonic Charge-Parity (CP) violation in the neutrino (ν) sector [4]. CP violation has already been searched and measured in the quark sector and found to be relatively small. If CP violation is found in neutrinos, it would help explain why our Universe has

[1] upgradable to 2.2 MW

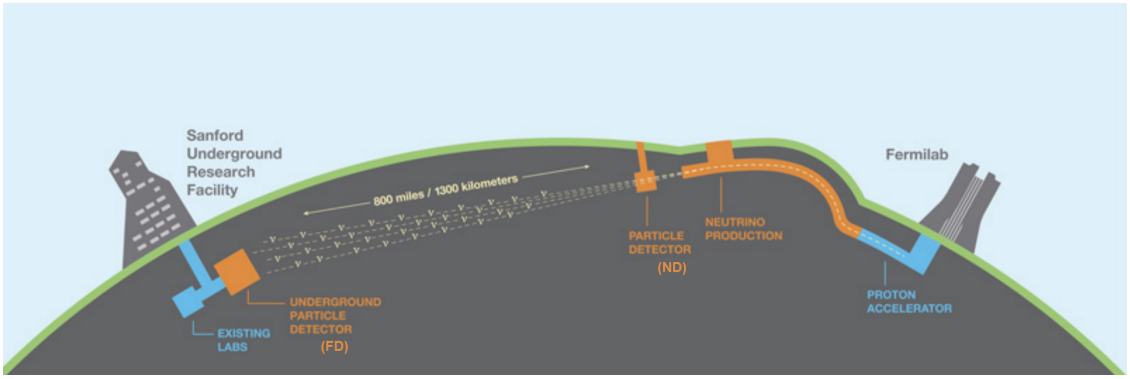

Figure 1.1: DUNE depiction. Beam travels right to left. Edited from [5].

a matter/anti-matter asymmetry. In the Standard Model, neutrinos are massless, but experimentally neutrinos have been measured to oscillate between 3 primary leptonic flavors (electron (e), muon (μ), tau (τ)), implying that neutrinos have a non-zero mass and as such, they are the first evidence of physics beyond the standard model.

If we can show that neutrino's anti-matter counterparts, anti-neutrinos, oscillate differently between the 3 neutrino flavors, then scientists can measure the CP-violating phase.

1.2 Neutrino Oscillation

Using the 2 flavor model, as a starting point to make the formulas easy, we can start to define the oscillation probabilities that DUNE is interested in. We can assume oscillation in a vacuum, as matter-effects only swap parameters in Eq. 1.1 for matter-modified versions. So the probability that a neutrino oscillates from one flavor α to another flavor β is given as:

$$P(\nu_\alpha \rightarrow \nu_\beta) = \sin^2(2\theta)\sin^2(1.27\Delta m^2 \frac{L[m]}{E[GeV]}) \tag{1.1}$$

Where θ is the mixing angle, a description of mass-to-flavor states. Δm^2 is the mass squared difference between two neutrino states, where nonzero implies neutrinos have (different) mass. L is the distance between near and far detector, and E is the energy of the neutrino. L/E is a parameter used in neutrino oscillation experiments to determine and select a particular region (phase space) for oscillation probabilities[2].

If we extend the model to three neutrino flavors, the general probability of a neutrino oscillating from one flavor α to another β becomes:

$$\begin{aligned} P(\nu_\alpha \to \nu_\beta) = \delta_{\beta\alpha} - 4 \sum_{k>j} Re[U^*_{\alpha k} U_{\beta k} U_{\alpha j} U^*_{\beta j}] \sin^2 (\Delta m^2_{kj} \frac{L}{4E}) \\ + 2 \sum_{k>j} Im[U^*_{\alpha k} U_{\beta k} U_{\alpha j} U^*_{\beta j}] \sin (\Delta m^2_{kj} \frac{L}{4E}) \end{aligned} \tag{1.2}$$

Where δ is Kronecker delta. U is the PMNS consisting of 3 complex phases scattered amongst 3 rotation matrices and a Majorana phase matrix. U* is defined as the conjugate transpose of U. The "13-sector" rotation matrix carries the CP Violation (CPV) phase which propagates through derivations to form the Imaginary term in Eq. 1.2. To search for any CPV, we can set the CPV phase to zero, therefore assuming/testing a no-CPV model. So the CPV phase drops and by consequence the Imaginary term drops, leading to

$$\begin{aligned} P(\nu_\alpha \to \nu_\beta) = \delta_{\beta\alpha} - 4 \sum_{k>j} Re[U^*_{\alpha k} U_{\beta k} U_{\alpha j} U^*_{\beta j}] \sin^2 (\Delta m^2_{kj} \frac{L}{4E}) \\ + 0 \end{aligned} \tag{1.3}$$

[2]One exception to this is the solar neutrino experiments in which L/E is fixed.

Eq. 1.3 is the governing equation for accelerator neutrino experiments where the probability of oscillation is still intimately coupled with the ratio L/E. We measure the number of un-oscillated events very close to the neutrino source and then the number of oscillated events at the detector. In the case of DUNE, the un-oscillated events are measured at the ND and the oscillated events are measured at the FD (so that L = 1,300 km) [6]. The ratio between far and near detector events is the probability of neutrino oscillation.

It is important to note that there is a hidden signal in this vacuum oscillation picture, since the oscillation at DUNE occurs in the Earth. Beyond the CPV-phase term, there is a matter-effect addition to Eq. 1.2 and 1.3 which produces a CPV signal that is necessary to decouple. It is sufficient to first choose a large distance that captures the L/E dependence in Eq. 1.3 but not so large as to allow the matter-effect to dominate, and secondly to identify/reconstruct the (anti-)neutrino flavor/energy [7].

It is then possible to test CP symmetry conceptually by looking for an Asymmetry, defined as:

$$A_{CP} = \frac{P(\nu_\alpha \to \nu_\beta) - P(\bar{\nu}_\alpha \to \bar{\nu}_\beta)}{P(\nu_\alpha \to \nu_\beta) + P(\bar{\nu}_\alpha \to \bar{\nu}_\beta)} \tag{1.4}$$

That is, after calculating the experimentally defined probability for a neutrino or anti-neutrino to oscillate, if Eq. 1.4 takes a non-zero value, then there is evidence for an asymmetry and therefore CPV. To find $P(\nu_\alpha \to \nu_\beta)$ experimentally, it is necessary to take the ratio of the event rates measured between near and far detectors. The number of events at the near and far detectors are defined as

$$N^{\alpha}_{ND}(p_r) = \sum_i \phi_\alpha(E_{true}) \cdot \sigma^i_\alpha(p_{true}) \cdot \epsilon_\alpha(p_{true}) \cdot R_i(p_{true}; p_r)$$
$$N^{\alpha\to\beta}_{FD}(p_r) = \sum_i \phi_\alpha(E_{true}) \cdot P_{\alpha\beta}(E_{true}) \cdot \sigma^i_\beta(p_{true}) \cdot \epsilon_\beta(p_{true}) \cdot R_i(p_{true}; p_r) \quad (1.5)$$

where p_r is defined as the reconstructed 4-vector energy-momentum $(E_r, \vec{p_r})$, p_{true} is defined as the true 4-vector energy-momentum which is inherent to the neutrino, $N^{\alpha}_{ND}(p_r)$ is the measured event rate for ν_α at the ND, $N^{\alpha\to\beta}_{FD}(p_r)$ is the measured event rate for ν_β at the FD after an oscillation from ν_α at the ND, ϕ_α is the flux of α neutrinos at the ND, σ^i_l is the flavor l neutrino cross section for an interaction i, ϵ_l is the detector efficiency for flavor l neutrinos, and R_i is the probability that p_{true} is reconstructed as p_r given an interaction i and some encoded detector or nuclear effect on the final state has taken place [7]. $P_{\alpha\beta}$ is the probability that a neutrino with true energy will oscillate from α to β and is the component we want to capture by taking the ratio of the near and far event rate in Eq. 1.5.

So two detectors, the ND and FD, with known distance are theoretically sufficient. The far detector rates will be compared against the near detector rates to indicate the high-precision neutrino flavor oscillation for possible CPV [4, 6]. However, these measurements require fully understanding the incoming neutrinos and their energy, which is famously difficult to measure directly. The neutrinos require reconstruction, and their reconstructed energy, along with the event rates themselves, are reliant on the cross section and type of interaction that takes place [7].

The neutrinos have to be reconstructed by looking at all the outgoing particles from the initial neutrino interaction. So the DUNE's goal of measuring the CPV phase with high precision requires precise knowledge of neutrino interactions with a complex nuclei. As Argon nuclei

are the main targets for neutrino interactions at DUNE, Argon has to be fully understood. Therefore, a parameter-free model of the neutrino-nucleus interaction for the Argon inside LArTPCs is required. To achieve this model, a deeper understanding of Argon's protons and neutrons is necessary for current and future neutrino oscillation experiments like DUNE.

How individual protons and neutrons behave in lepton-nucleus interactions is tied in part to their energy-momentum distribution inside the nucleus. The method of knocking out the individual nucleons allows researchers to gauge the level of energy required to remove said nucleon and probe its inherent momentum. One model to describe such interaction is the Spectral Function model which can determine the probability of extracting a single nucleon with a certain energy and momentum from a given nuclei. If a nucleon is believed to have a range of allowed momenta inside a nucleus with a shared Energy [3], then the Spectral Function gives us some likelihood that the nucleon is removed and the remaining nucleus has a new energy [8].

1.3 Electron-Nucleus Scattering

Traditional nucleon knockout is performed with an electron beam scattering experiment [9]. Electrons, at least our current understanding of them, have the benefit of being an elementary particle and favorably follow electroweak interactions through space-like photons. This allows us to effectively strike (and therefore probe) deeper into the bound energy states of the nucleus [10, 11]. Due to the fact that electrons are negatively charged, they are also relatively easy to track, filter and detect. For comparison, using a proton beam to strike the nucleus is more complex since the proton is a composite particle that follows strong interactions. Restricted by the interference of this strong interaction, we would mainly be

[3] here we are assuming the system is in the ground state

relegated to largely surface level probes of the nucleus, before competing effects would introduce substantial noise and require significant separation [12]. It is this reason historically that electron scattering is performed prior to proton scattering to sufficiently specify the nuclear structure [13]. So utilizing an incident electron beam is easier and more practical in kinematic modelling. Therefore, electrons were chosen for this experiment.

Argon is isospin asymmetric (the number of protons does not equal the number of neutrons), and the energy-momentum levels (or shell states) accessible to one nucleon is not the same /mirrored in the other Fig. 1.2. Probing protons is theoretically straightforward. Given the proton's charge, it is relatively easy to track, filter and detect alongside the electron after knockout.

Neutrons, a neutral particle, are difficult to track and measure. They require indirect methods to measure through the release of other charged particles: typically described as ionizing a target detector or causing a nuclear reaction and measuring the products of the fission [14]. You effectively have to measure the neutron and its reactions. In fact, due to these difficulties, a major correction has to be done to account for the nucleons' self-interactions [15]. A neutron can elastically rescatter off the nucleus. A rescatter known as charge-exchange can also take place. In this rescatter process the neutron is not actually produced at the elementary interaction vertex. That is to say a proton could have been knocked loose by the electron beam, but the proton is still energetically favorable to interact with a neutron in the remaining nucleons. This proton then effectively trades places (is exchanged) with the neutron it knocks out. Detectors are already measuring the neutron indirectly, and now have to account for the fact that the neutron may or may not be a rescatter byproduct. Additionally, the detection efficiency for neutrons is much smaller than for protons[4] when the cross section for neutrons is already 10% that of protons [16]. So these restrictions made

[4] order 20%

precise (e,e′n) experiments in medium-to-heavy nuclei uncommon until recently [17].

One workaround of the difficulties introduced by the neutron analysis is to use the assumption of isospin symmetry of nuclear forces[5]. If we can probe protons easily, then we simply need to find a nucleus whose protons can mimic the levels allowed for Argon's neutrons. In other words, use Titanium, a nucleus with the same number of protons as Argon has neutrons Fig. 1.2. Working forward from isospin symmetry, we can use Titanium proton knockout measurements as a proxy for Argon's neutron measurements (and the ensuing Spectral Function) [18].

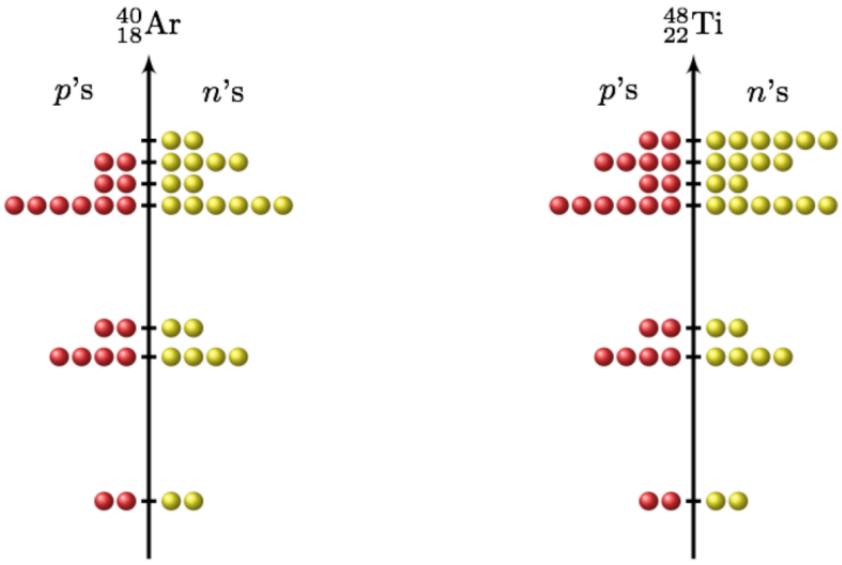

Figure 1.2: Nuclear shell model of Argon and Titanium. Titanium's proton shell states (p's) are portrayed as a mirrored reflection of Argon's neutron shell states (n's). This conceptual analogy is the basis for measuring Ti(e,e′p) in place of Ar(e,e′n)

.

[5]isospin has an approximate symmetry, due to being broken by coulomb forces, different charges, and mass differences [19]

1.4 Exclusive (e,e′p) reaction

The (e,e′p) scattering is an exclusive scattering as we can detect all the final particles and determine their momentum and energy. Fig. 1.3

$$e + A \rightarrow e' + p + (A-1)^* \tag{1.6}$$

in 4-vectors notation (with respect to natural units $\hbar = c = 1$), we can define:

- The incoming electron (e^-) as having energy-momentum of (E, $\overrightarrow{k}$).
- The nucleus (A) which is assumed to be at rest in the lab frame so it is described by (M_A,0) where M_A is the rest mass of the nucleus.
- The outgoing electron (e′) would have (E′,$\overrightarrow{k'}$) which is measured directly.
- Through simple conservation of energy-momentum, the energy-momentum transferred (via the electroweak messenger, the photon) to the nucleus (A) is (E,$\overrightarrow{k}$)-(E',$\overrightarrow{k'}$) = (ω,$\overrightarrow{q}$).
- The proton (p) that is knocked out would have some initial energy-momentum component of the nucleus (recall, what we're really curious about), and chiefly for the experiment a final energy-momentum after knockout given as (E_p,$\overrightarrow{k_p}$) which is measured directly,
- Leaving the residual nucleus (A-1) to recoil inside some residual system we will define with (E_{A-1},$\overrightarrow{p}_{A-1}$).

On the topic of measuring directly, it should be noted that it is the momenta that are typically measured in these experiments. For this model, we will treat the energy components through

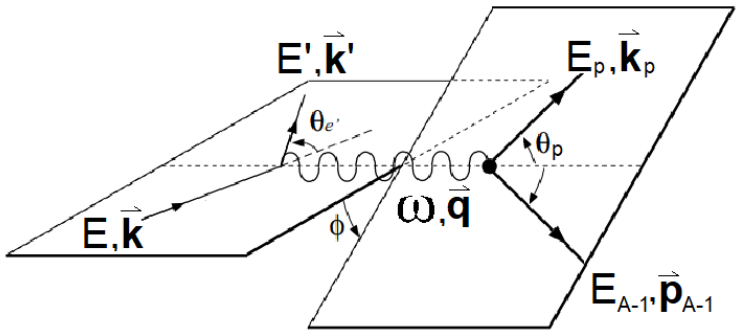

Figure 1.3: Kinematic schematic of the (e,e′p) reaction. Replicated from [20].

assumptions. Starting with the relativistic dispersion relation, the proton's energy is given as $E_p = \sqrt{M_p^2 + k_p^2}$ where M_p is the proton's rest mass. The electrons in the beam are within the ultra-relativistic regime (k»M) and so their energies are simply approximated with their rest mass neglected (i.e., E ≈ |k|).

As stated, we are interested in the proton energy-momentum distribution inside the nucleus, but unfortunately it is difficult to measure. Thankfully, with our collision listed above, we can piece together this distribution through a quantity known as missing energy-momentum.

The missing energy is defined as

$$E_{miss} = \omega - T_p - T_{A-1} \tag{1.7}$$

where T_p, T_{A-1} are the relativistic kinetic energies for the proton and the recoil system respectively.[6] The missing energy gives us a useful starting point. We can start by explicitly

[6]The equation above is more accurately described as missing mass $E_{miss} = m_p + m_{A-1} - m_A$ (as is the case with a lot of conventions that utilize natural units, mass is measured by energy). Other collaborations also define the missing energy differently, preferring to drop the residual term [15]. Great care should be taken in the future when comparing high-precision data.

writing out the residual mass as $m_{A-1} = \sqrt{E_{A-1}^2 + p_{A-1}^2}$. Using the conservation of energy:

$$\begin{aligned} E + M_A &= E' + E_p + E_{A-1} \\ &OR \\ E_{A-1} &= \omega + M_A - E_p \end{aligned} \tag{1.8}$$

so we can rewrite the missing energy 1.7 as :

$$E_{miss} = m_p - M_A + \sqrt{(\omega + M_A - E_p)^2 - p_{A-1}^2}. \tag{1.9}$$

However, Eq. 1.9 still depends on the momentum of the residual system. To replace the momentum, the last step is including conservation of momentum:

$$p_p - q = -p_{A-1} \tag{1.10}$$

where the negative signs can be taken as purely convention, as Eq. 1.10 is defined to be the missing momentum (i.e., the recoil momentum, or the momentum the proton had prior to knockout).

So putting together Eq. 1.9 and Eq. 1.10 our missing energy-momentum is now a testable expression that does not require any measurements of the residual/missing information. Anything not observed in the incoming or outgoing particles can be interpreted as missing due to an interaction with the nuclear states that ejected the proton.

1.5 Spectral Functions

After measuring quantities and inferring missing portions, it is necessary to assess those values with the help of statistical analysis.

What we want to capture from this scatter is the (e,e′p) cross section. The cross section allows us to measure the spectral function of the nucleus, an intrinsic value given as P($\overrightarrow{p}_{miss}$,$E_{miss}$). This spectral function represents the probability of removing a nucleon (here a proton) with Energy-momentum (E,$\overrightarrow{p}_{miss}$). More explicitly, this Spectral function represents the probability that a nucleon with momentum $\overrightarrow{p}_{miss}$, and bound with energy E to an initial shell state inside the target nucleus (A), is removed and left the residual nucleus (A-1) in any final state with missing energy E_{miss} [15]. Therefore, when indirectly measuring some missing quantity, only direct measurements are require to determine the initial state.

The preceding prescription pertains to ideal conditions. However, The proton does not always escape its initial state undisturbed. We have been approximating the proton as a plane wave in the Plane Wave Impulse Approximation (PWIA) treatment. Electron scattering that facilitates a nucleon knockout comes close to PWIA, so there are only minor corrections to make. These corrections account for the Final State Interactions (FSI) that describe the ways in which the proton and residual nucleus can self-interact before measurement. Including FSI "distorts" the PW, hence the name Distorted Wave Impulse Approximation (DWIA). While still assuming that the electron is initially only interacting with one proton, DWIA can get quite complicated. Thankfully, if we operate under parallel-kinematics[7] , then we can approximately "factorize" terms, leading to a factorized DWIA [21, 22, 23]. Furthermore, we are working under the assumption that the beam-target interaction involves a single nucleon and that any FSI can be described by a single potential in DWIA. Following this route, we

[7]all kinematics chosen in this experiment are within this regime

have the factorized DWIA cross section as a six-fold differential [24] :

$$\frac{d^6\omega}{d\omega d\Omega_{e'} dT_p d\Omega_p} = K\sigma_{ep} P^D(\vec{k}_p, \vec{p}_{miss}, E_{miss}) \tag{1.11}$$

On the left hand side of Eq. 1.11, ω and T_p respectively correspond to the photon energy transfer and proton kinetic energy described previously, as in Eq. 1.7. Ω'_e and Ω_p respectively represent the solid angle directions of the outgoing electron and proton.

On the right hand side of Eq. 1.11, K is the kinematic factor and it is equal to $K = |p'|E$. σ_{ep} is the differential cross section for an electron to scatter off a bound and moving proton and P^D is the distorted spectral function[8].

And we can rewrite the six-differential cross-section of Eq. 1.11 as:

$$\frac{d^6\omega}{d\omega d\Omega_{e'} dT_p d\Omega_p} = \frac{Y(E_{miss}, p_{miss})}{B \cdot lt \cdot \rho \cdot BH \cdot V_B \cdot C_{rad}} \tag{1.12}$$

Where the right hand side of Eq. 1.12 are physical parameters measured throughout the experiment (Y, B, lt, ρ, BH) and simulated in SIMC (V_B, C_{rad}) [24, 46].

Setting 1.11 and 1.12 equivalent allows us to isolate the distorted spectral function. It is then a matter of isolating the nucleon spectral function by removing the FSI distortion effects from P^D. Associated with the distorted spectral function is a reduced cross section. This is found by dividing out Kσ_{ep} from the measured cross section. This is compared against a reduced cross section generated by Monte Carlo via a test Spectral Function [24]. The test Spectral Function is a weighted decomposition of independent-shell contributions[9] and the correlated nucleon pairs[10]. This test spectral function construction allows the individual shell

[8] Note: no longer intrinsic to the nucleus, the SF now depends on the exiting nucleon.
[9] assumed to follow a Gaussian distribution for all proton orbitals
[10] assumed to be short-range proton-neutron pairs in a convolution integral of Gaussians

contributions to be separated. Through separation, the shells can be compared to data in order to ascertain if the remaining correlated contribution produced a precise representation of the system's FSI.

Chapter 2

Jefferson Lab Experimental Hall A

The JLab experiment E12-14-012 was approved by the Jefferson Lab PAC in 2014 and data was taken in Spring 2017. In the past few years, a series of measurements have been completed: the inclusive, (e, e′) [25, 26, 27], and exclusive (e, e′p) [24, 28] electron scattering cross sections on several targets, including a natural gas argon target [24, 28].

As stated in Ch. 1's description of the nucleon knockout, we are searching for the missing energy-momentum that describes our target. This means that all other participants in the knockout process must be precisely measured. The apparatuses that perform the scattering measurements are housed in Hall A at JLab. Figure 2.1 shows a broad overview of the Hall A setup at JLab.

We begin with our incident particle, an electron beam of 2.2 GeV and $\approx$ 22 µA that is provided by the Jefferson Lab Continuous Electron Beam Accelerator Facility (CEBAF).

Electrons are injected onsite and accelerated up to the desired energy level before being extracted and sent to the beam switch-yard, where they are perturbed into the "ARC" towards Hall A and into the ensuing experiment. The knockout proton (from the target) and scattered electron are detected in coincidence by two specialized high-resolution spectrometers (HRSs), respectively designated Right and Left.

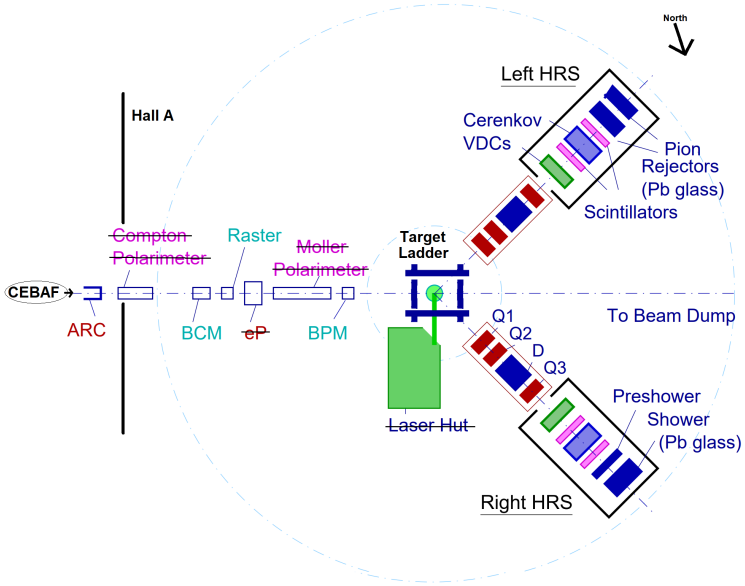

Figure 2.1: Floor Plan of Hall A. Not to scale. Experiment utilized standard equipment. Polarimeters and eP method not utilized during experiment run. Replicated from [29].

2.1 Experimental Measurements of beam energy and momentum

Starting from the electron's extraction, we begin with the first precise measurement of the beam energy-momentum. The so called 'arc method' is a means to determine what is being sent upstream to the experiment. For a greater description of the method, see [20] . To summarize the method: as electrons, with some momentum, pass through magnetic fields they will be influenced into following a circular arc. So we can reverse engineer the momentum[1], as given in Eq. 2.1, so long as we measure the magnetic field, the path length, and the arc section/angle that the electrons were deflected by.

$$p = |e| \frac{\int_0^l \vec{B} \cdot d\vec{l}}{\theta} \tag{2.1}$$

[1]The Energy can be related to the momentum with the ultra-relativistic approximation.

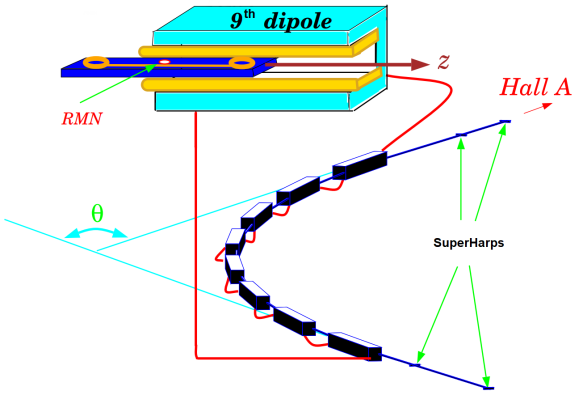

Figure 2.2: ARC Method. Replicated from [20]

The arc is outfitted, chiefly, with 8 dipoles (a.k.a. dispersive mode[2]) all of equivalent magnetic strength and parallel faces that bend the electron beam towards Hall A. See Fig. 2.2 for reference.

The use of a 9^{th} dipole in series [30] allows us to determine the magnetic field and path length combined in Eq. 2.1's numerator (the so-called field-integral). Eq. 2.1's denominator is the deviation angle, the nominal value of which is 34.3° set by the experiment. $|e|$ in Eq. 2.1 is the absolute value of the fundamental electron charge[3].

On the electron's path through the ARC, the nominal angle can be further verified through measurement using the so-called Superharps. The Superharps are sets of wires that are moved across the beam path and create a signal that is picked up by PhotoMultiplier Tubes (PMTs). It should be noted that the Superharp angle measurement is rather invasive; therefore, Superharps are primarily a diagnostic tool. In actual experiment runs, BPMs (discussed later) are the primary tool to measure position and direction of the beam.

[2]The arc comes equipped with quadrupoles, which when turned on is known as achromatic mode. The quadrupoles are meant to precisely align the beam, and so higher order corrections could be made, however dispersive mode is primarily used for energy measurement checks- not achromatic (which is only alignment/focus).

[3]often in place of e will be a k, which is a mathematical artifact given by electron charge and energy relations through the derivation, as in Ref. [20]. Using natural units, k is approximately .299 GeV $T^{-1}m^{-1}$ and indicates Eq. 2.1 is referring to energy rather than strictly momentum.

Continuing into Hall A, the electron beam would pass through the first of two polarimeters. However, the polarity of the electron beam is not significant to the experiment's results. So neither polarimeter is in use during the experiment's run.

2.2 Determination of the Beam Intensity

Next in line to the target is the Beam Current Monitor (BCM) [31, 32, 33] , which reads an incoming current, and therefore intensity. The intensity measurement is not only needed for the kinematic picture, but is also utilized in describing beam effects such as the "boiling effect" in strongly affected systems like our Argon Target. The beam heats up the gas target and can create different density pockets inside the target, affecting the number of interactions [34] . The BCM system consists of several redundant monitors that measure the beam's charge every second[4] while accumulating the total charge for the run. The primary non-invasive monitors are calibrated by an absolute reference whose output drifts over time. So an invasive calibration[5] needs to take place on the order of every 1-2 months. However, low current (<50 μA) runs such as in this experiment can require an invasive calibration on the order of once or twice a month. With the calibrations in place, an accuracy of 0.5% can be achieved for currents $\in$ [1,180] μA, although it has been previously shown that 0.2% accuracy is possible [31].

2.3 Diffusing beam on target - Raster

Further downstream in Fig. 2.1 is the raster system which spreads the beam over the target to avoid melting the target due to concentrated beam current densities. Rastering also lowers

[4] which can be interpreted as the average current over the same timescale
[5] about 1/2 hr long

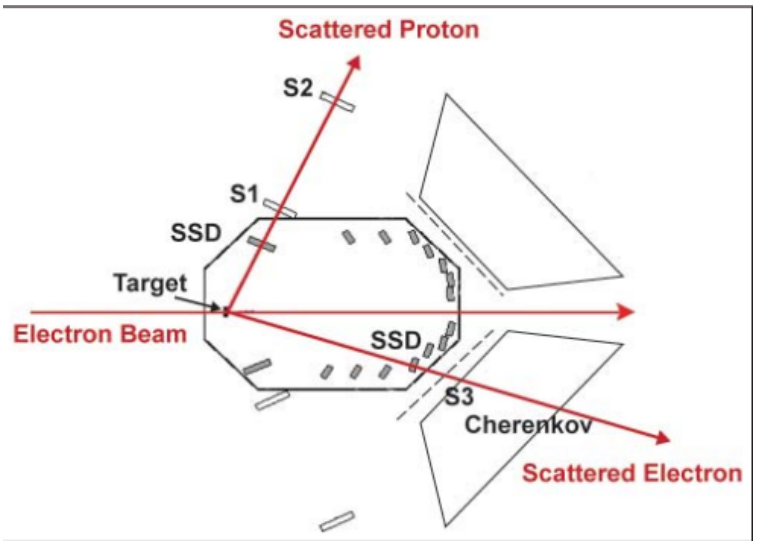

Figure 2.3: eP method [35]. Diagnostic tool to measure energy, not directly utilized for experiment.

the boiling effects on the target. The raster area on our target was 2×2 mm^2.

2.4 eP method

Another invasive measurement is the eP method, see Fig. 2.3, that relies on the exclusive H(e,e′p) scatter/knockout. The eP method is a diagnostic tool not utilized in the experiment run, but worth describing as it gives a meaningful benchmark for Hall A's energy readings, and it follows a similar scheme as the experiment's knockout HRS measurement. The incident beam scatters off a reliable target with a high hydrogen concentration (to reduce noise from the beam scattering off heavier nuclei[6]). The eP detector system involves a symmetric[7] design of two so-called arms- consisting of proton and electron capture devices. The nature of the kinematic reaction sets the proton scattering angle, and a single Silicon-Strip Detector (SSD) is set to capture this angle. Two accompanying scintillators provide time of flight and

[6] CH_2 is one such target
[7] With respect to the beam, along the vertical plane

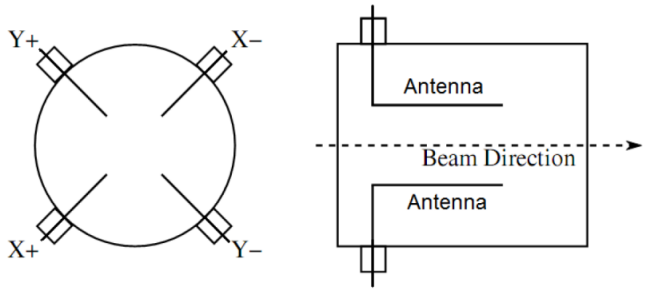

Figure 2.4: Beam Position Monitor (BPM). Left: Beam view. Right: Side View. [36]

triggering for the scattered proton[8]. The electron angle is more dependent on the incoming energy, therefore seven SSDs are positioned so that at least one can capture the intended angle. A Čerenkov counter and scintillator pairing are used for the electron triggering[9]. With the electron and proton scatter angles measured, the beam energy can be determined, see [30].

2.5 Beam Position Monitor (BPM)

As stated earlier, the BPMs provide relative measurements of position. There are two identical BPMs upstream of the target [33], and one is portrayed in Fig. 2.4. A BPM consists of four wires, bent to act as antennas parallel to the beam, measuring the beam's current through an induced current. The strength of the induced current in the wire is proportional to the distance from the beam. So a beam position can be determined by constructing an axial system with the information collected from the four wires. It should be noted here that if any directional comparisons are to be made, Hall A utilizes four separate coordinate systems portrayed in Fig. 2.5.

[8]The SSD and two scintillators will be symmetrically mirrored
[9]again, the Čerenkov counter and scintillator will be symmetrically mirrored

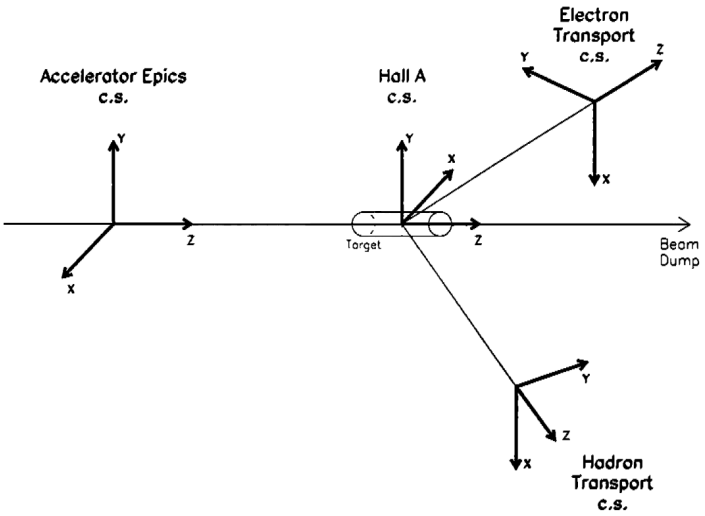

Figure 2.5: Coordinate Systems (c.s.) at JLab. Side View. All c.s. have traditional z-axis downstream. Both Accelerator and Hall A c.s. have the y-axis pointing upward towards the vertical. The transport c.s. are antiquated terms referring to the now HRSs c.s. and have their x-axis point downward along gravity. The Accelerator c.s. is left-handed and the remaining three c.s. are right-handed. Replicated from [37].

2.6 Hall A Target system

Having covered all the equipment prior to the target, we now have precise measurements on the incoming electron described in our kinematic prescription[10]. The quantified beam is now incident on the target, or rather the whole target system (a.k.a. target ladder) designed for this experiment. The target system is a series of targets, like rungs on a ladder, that can be moved into the beamline as needed. See Fig. 2.6 for a sample image of a target configuration.

First and foremost are the titanium and argon targets. The isolated titanium target consists of a foil with (mass) thickness of 0.73 g/cm^2 and substitutes argon in determining neutron knockout.

[10]Recall, energy of the beam was the first important factor to determine from our model.
With the beam position also known in a non-invasive manner, the knockout vertex can be defined further down stream.

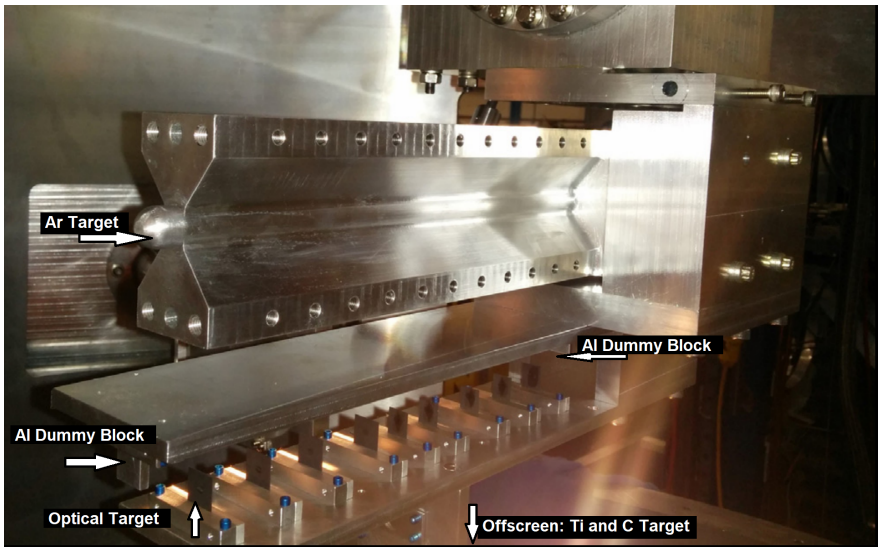

Figure 2.6: Photograph sample of Hall A Target Ladder. From top to bottom: Target Cooling system attached to the Al cell filled with Ar, a plate with the Al Dummy Blocks attached underneath, the 9 C Optical Targets, and off-screen are the Ti and C foil targets. Replicated from [34].

The argon target is a closed gas cell made of aluminum. The argon target is maintained around 291 K, 3.45 MPa and 58.2 kg/m^3, however as described earlier a boiling effect occurs due to the beam depositing heat which has to be accounted for [34]. The aluminum cell is a 25 cm long[11] tube with an inner diameter of 12.7 mm and wall thickness of 0.4-0.5 mm. The entrance/exit windows are capped with aluminum of thickness 0.25 mm.

Due to the aluminum housing being a source of background, electrons can in fact interact in the aluminum of the target. For this reason, a dummy target is added to the system to determine the number of interactions happening in the aluminum. This dummy target consists of only two blocks of aluminum, separated by 25 cm and each with thickness of 0.889 g/cm^2. This dummy target is then used to determine the background caused by the argon's aluminum housing, and as an added bonus can also be used to calculate the Al(e,e$'$) cross section.

[11] along the beam

An isolated carbon foil target with thickness 0.35 g/cm^2 is also installed in the target ladder system. Carbon data is readily available, so this carbon target is used to measure the inclusive C(e,e$'$) cross section and verify the analysis procedure against existing data.

Finally, an "optical target" consisting of 9 carbon foils with thickness of 0.35 g/cm^2 are positioned at z = $\pm\{0,\ 2,\ 5,\ 7.5,\ 10\}$ cm. The optical target's purpose is to align and calibrate the spectrometer optics.

2.7 High Resolution Spectrometers - HRS

Upon reaching the target, the beam can pass completely through and proceed to the "Beam Dump". In the standard configuration, the Beam Dump is simply a series of aluminum absorbers enclosed in concrete and cooled by a circulating water heat sink.

However, the primary collision of interest may take place and so the outgoing protons and electrons are then detected by the HRSs. The Hall A HRSs can be rotated[12] into position for the expected outgoing angles. As the scattered electrons and knocked-out protons exit the beamline, they proceed to their respective HRS.

Each HRS has a magnet configuration to bend charged particles toward their detectors. The magnets consist of three quadrupole (Q) magnets and one dipole (D) magnet in the QQDQ configuration shown in Fig. 2.7. The magnets produce a 45° bending angle while improving resolution by focusing the particles [38] . See Table 2.1 for a list of HRS features.

Both HRSs are equipped with vertical drift chambers (VDCs) [39] to track the particles through path reconstruction [33]. The position resolution in the focal plane is $\approx 100\ \mu$m and the angular resolution is ≈ 0.5 mrad. Following the VDCs, in each HRS, are two scintillators

[12] pivoted about the target as the center

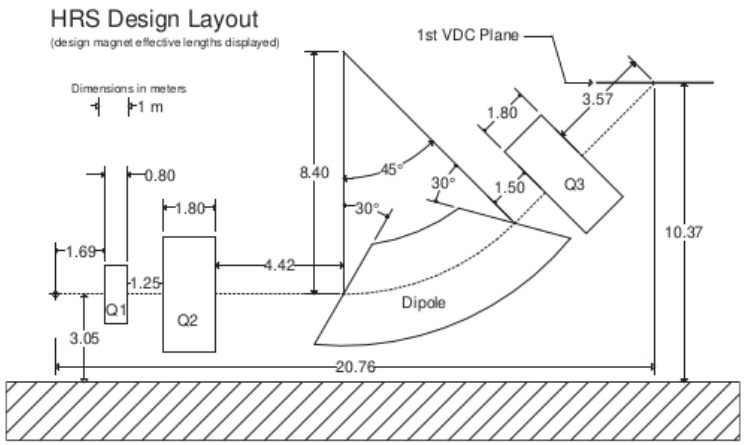

Figure 2.7: HRS QQDQ and VDC orientation schematic. Dashed line is approximate beamline, entering from left and bending upward towards the 1st VDC Plane [33].

read by PMTs. The scintillator pairs allow for time of flight and particle speed measurements while providing the detector with a trigger for reading. Between the scintillators is a gas Cherenkov detector with accompanying mirrors and PMTs, whose design differed[13] between the HRS-L and HRS-R [33]. The Cherenkov detector is used as an electron detector and pion rejector. The threshold for a pion to produce Cherenkov light is above the expected value of a pion produced in this experiment. Whereas the threshold for an electron to produce light is well within the experiment's parameters. So a lack of light is a useful indicator that a pion event has taken place and should be rejected. At the end of each HRS are two layers of lead glass blocks [33]. The layers are designed as a pair to be a calorimeter and shower detector. The calorimeter measures electron and proton energies through accompanying PMTs that measure produced light. Pions are less likely to interact with the lead blocks; therefore, the lead blocks, in conjunction with the Cherenkov detector, act as a pion rejector. Like the Cherenkov detector, the calorimeters in each HRS are designed differently. This difference amounts to a greater path length and resolution in HRS-R over HRS-L.

[13] primarily in path length

Table 2.1: Hall A HRSs [33].

Configuration	QQD_nQ Vertical bend
Bending angle	45°
Optical length	23.4 m
Momentum range	0.3 - 4.0 GeV/c
Momentum acceptance	$-4.5\% < \delta p/p < +4.5\%$
Momentum resolution	2×10^{-4}
Angular acceptance (Horizontal)	±30 mrad
Angular acceptance (Vertical)	±60 mrad
Angular resolution (Horizontal)	0.5 mrad
Angular resolution (Vertical)	1.0 mrad
Solid angle at $\delta p/p = 0$, $y_0 = 0$	6 msr
Transverse length acceptance	±5 cm
Transverse position resolution	1 mm

Chapter 3

(e,e'p) on Ar - Data analysis overview

We have performed exclusive analysis for E12-14-021 Ti data. The titanium analysis has been published in Physical Review D [40], and it is presented in Ch. 4 as it appears in the publication. The exclusive analysis for E12-14-021 argon data was performed by L. Jiang, et al. [24] and will be reviewed in this chapter separately. The two analyses follow the same methodology [24, 28]; therefore, the argon data is used to present the framework that will be utilized in the titanium analysis.

As described in Ch. 1, a test spectral function needs to be constructed to be able to generate simulated data to compute efficiency and backgrounds.

The $(e, e'p)$ events in our experimental setup were simulated using the JLab SIMC [46] package. Such simulation included detailed simulation of the target cell, radiation corrections, and Coulomb effects[1]. SIMC needs a spectral function as an input to effectively weigh the simulated events and generate distributions of the missing energy and momentum.

The test spectral function is the sum of two components, the mean-field (MF) and the correlated (Corr.) parts: [24]:

$$P(p_{miss}, E_{miss}) = P_{MF}(p_{miss}, E_{miss}) + P_{corr}(p_{miss}, E_{miss}) \tag{3.1}$$

[1]SIMC does not include FSI corrections other than nuclear transparency. Further details on including FSI can be found in [28]. For now, we should expect expect the Monte Carlo simulations typically to overestimate the data. A typical effect of FSI is a reduction of the cross-section.

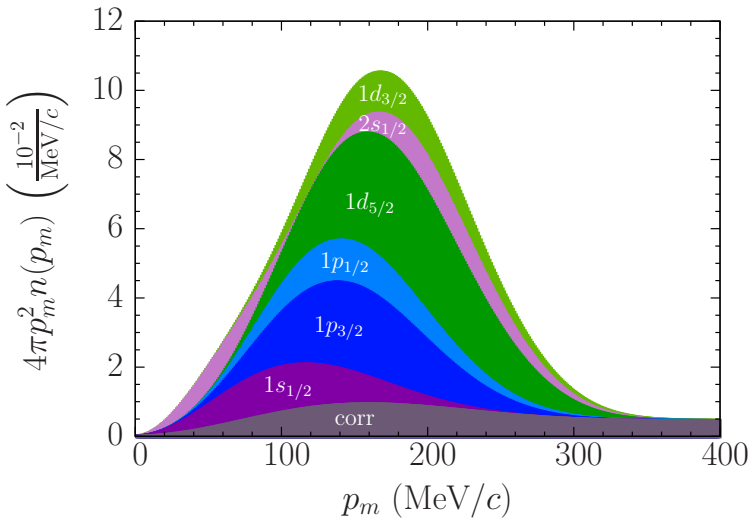

Figure 3.1: Simulated missing momentum distribution of the various proton shell in argon [24].

The MF component is a sum over the expected occupied states (α) in the independent-particle shell model [24]:

$$P_{MF}(p_{miss}, E_{miss}) = \sum_{\alpha} S_\alpha |\phi_\alpha(p_{miss})|^2 f_\alpha(E_{miss}), \tag{3.2}$$

where S_α are the spectroscopic factors of each proton state α, $\phi_\alpha(p_{miss})$ is the momentum-space wave function (unity normalized) of the state α, and $f_\alpha(E_{miss})$ represents the distribution of missing energy, assumed to have the following Gaussian distribution:

$$f_\alpha(E_{miss}) = \frac{1}{\sqrt{2\pi}\sigma_\alpha} e^{-\left(\frac{E_{miss}-E_\alpha}{\sqrt{2}\sigma_\alpha}\right)^2}, \tag{3.3}$$

E_α is the peak value and σ_α expresses the width of the Gaussian distribution. Table 4.1 summarizes the values for the missing energy distribution of the shell-model state α peaked at E_α with a width of σ_α.

The correlated spectral function is approximated as a convolution integral involving a proton-

Table 3.1: Details of the test spectral function parameters for protons in argon.

α	N_α	S_α	E_α (MeV)	σ_α (MeV)
$1d_{3/2}$	2	1.6	12.53	2
$2s_{1/2}$	2	1.6	12.93	2
$1d_{5/2}$	6	4.8	18.23	4
$1p_{1/2}$	2	1.6	28.0	6
$1p_{3/2}$	4	3.2	33.0	6
$1s_{1/2}$	2	1.6	52.0	10
corr.	—	3.6	20.60	—

neutron (pn) pair:

$$P_{\rm corr}(p_{miss}, E_{miss}) = \int d^3p_{A-2}\, \delta\left(E_{miss} - E_{\rm corr} - T_{A-1}\right) n^{pn}_{\rm cm}\left(\left|p_{A-2}\right|\right) n^{pn}_{\rm rel}\left(\left|p_{miss} + \frac{p_{A-2}}{2}\right|\right) \tag{3.4}$$

where n_{cm} and n_{rel} refer to the momentum distributions with respect to center of mass and relative motion, E_{corr} is set to the pn knockout threshold, and T_{A-1} is the energy of the relative motion of the (A-2)+(correlated nucleon) system [24]. P_{corr} accounts for 20% of the total test spectral function strength. See Table 3.1 for the specific parameters.

Fig. 3.1 is the momentum distribution after including the correlation component computed using the wave functions from Ref. [41]. The test spectral function used in our simulation are presented in Fig. 3.2 as function of both the missing momentum and the missing energy.

The six-fold differential cross section in the MC can be determined from Eq. 1.11 and we used as σ_{ep} the $CC1$ parametrization from de Forest [42, 43].

We use a electron beam of energy 2.2 GeV, with two different beam currents: 15 μA for the Ar target and 25 μA for the Ti target. We make use of both Hall A HRSs to detect the electrons and protons in final state in time coincidence. The HRSs used configurations are detailed in Table 3.2.

In addition to the gas Ar target and the solid Ti foil, the experiment used a set of other

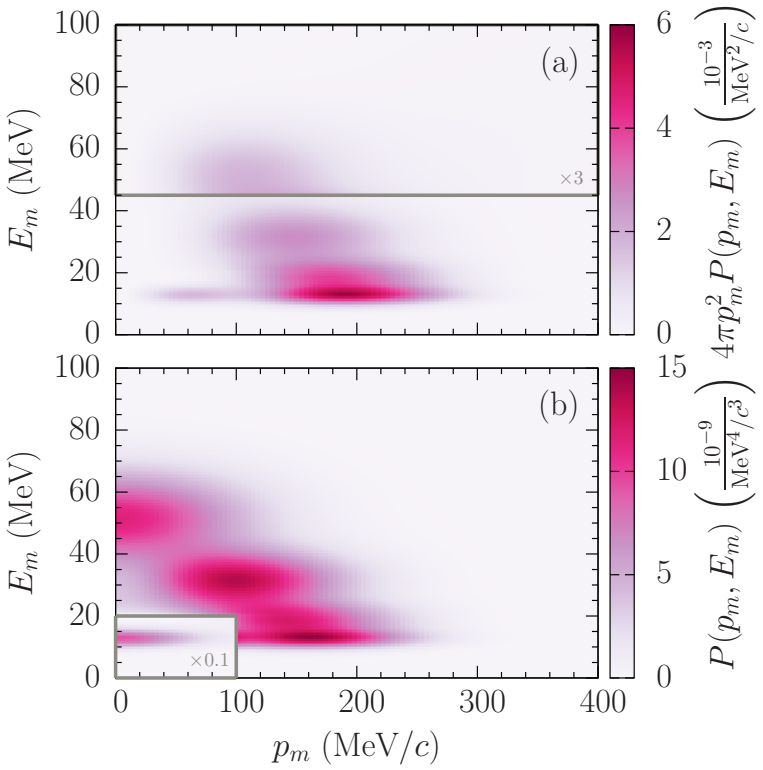

Figure 3.2: Strength of the test spectral function including (a) and excluding (b) the factor of $4\pi p_m^2$ [24].

targets as detailed in Ch. 2.

We used data from all kinematics settings as in Table 3.2 where E'_e is the final state electron energy, θ_e is the electron scattering angle, and p', $T_{p'}$, and θ_p are respectively the momentum, energy (kinetic), and angle of the scattered proton. p_m and E_m are the missing momentum and energy as defined in Ch. 2, while q and Q^2 are the momentum transfer and the squared of the four-momentum transfer. To be noted that our experiment took data exclusively with the vector q and P parallel to each other.

We used the VDC tracking information to measure the interaction vertex position, momentum and direction of the outgoing electron and proton. We made use of an optical matrix which was determined using data from the 9 carbon foils, to translate quantities between the focal plane and the target system [25, 26, 27, 28]. We have included systematic uncertainties

Table 3.2: Kinematics settings used to collect the data analyzed here.[24]

	E'_e (GeV)	θ_e (deg)	Q^2 (GeV$^2/c^2$)	$\|P\|$ (MeV/c)	$T_{p'}$ (MeV)	$\theta_{p'}$ (deg)	$\|\mathbf{q}\|$ (MeV/c)	p_m (MeV/c)	E_m (MeV)
kin1	1.777	21.5	0.549	915	372	−50.0	865	50	73
kin2	1.716	20.0	0.460	1030	455	−44.0	846	184	50
kin3	1.799	17.5	0.370	915	372	−47.0	741	174	50
kin4	1.799	15.5	0.291	915	372	−44.5	685	230	50
kin5	1.716	15.5	0.277	1030	455	−39.0	730	300	50

coming from both the optics and the magnetic field simulation for both the HRSs in our exclusive analysis.

The HRSs scintillator planes were used for triggering together with the gas Čerenkov (GC) detector, the pion rejector (PR), the pre-shower and the shower detector (PS) which were used to further refine the event selection [28]. Our event selection required events coming from the central region of the Ar target (±10 cm) in order to reduce background due to electron interactions in the Al of the gas cell. This kind of background was found to be negligible using our data and was also confirmed to be negligible by the tritium experiment at Jefferson Lab [34].

The various HRS detector efficiencies were studied in details and can be found in Ref. [25, 26, 27, 28] and also in Table 3.3 for both the Ar and Ti targets. The overall experimental efficiency was between 39.6% and 48.9% across all of our kinematics [28] and we used our MC to compute acceptances and efficiencies corrections [44]. Furthermore, we applied a correction for nuclear transparency [44, 45] and final state interactions (FSI) [28].

We extracted from the data the six-fold differential cross section as function of both p_m and E_m using Eq. 1.12.

The reduced cross section, as in Eq. 1.11, was derived dividing out the kinematic factor K

Table 3.3: Summary of the efficiency analysis for the argon data.

	Ar target	Ti target
a. Live time	98.0%	98.9%
b. Tracking	98.3%	98.3%
c. Trigger	92.3%	96.9%
d. Čerenkov cut	99.9%	96.6%
e. Calorimeter cut	97.8%	98.1%
f. β cut	95.6%	95.3%
g. Coincidence time cut	54.8%	55.5%

Table 3.4: Ar systematical uncertainties in %. For kin4 and kin5 the systematic is result of the sum (in quadrature) of systematic on both the signal and the background.

	kin1	kin2	kin3	kin4	kin5
1. Total statistical uncertainty	0.53	0.57	0.64	0.54	1.65
2. Total systematic uncertainty	3.14	3.24	3.32	10.23	9.01
a. Beam x&y offset	0.63	0.85	0.69	0.91	1.68
b. Beam energy	0.10	0.10	0.10	0.10	0.10
c. Beam charge	0.30	0.30	0.30	0.30	0.30
d. HRS x&y offset	0.83	1.17	0.78	1.44	1.71
e. Optics (q1, q2, q3)	0.94	0.77	0.55	0.90	1.72
f. Acceptance cut (θ, ϕ, z)	1.16	1.33	1.75	2.19	7.72
g. Target thickness/density/length	0.20	0.20	0.20	0.20	0.20
h. Calorimeter & Čerenkov cut	0.02	0.02	0.02	0.02	0.02
i. Radiative and Coulomb corr.	1.00	1.00	1.00	1.00	1.00
j. β cut	0.47	0.55	0.39	7.74	5.87
k. Boiling effect	0.70	0.70	0.70	0.70	0.70
l. Cross section model	1.00	1.00	1.00	1.00	1.00
m. Trigger and coincidence time cut	0.92	0.52	0.98	5.55	2.58
n. FSI	2.00	2.00	2.00	2.00	2.00

and the electron-proton off-shell cross section σ_{ep} [42, 43].

We measure the background events using events selected in anti-coincidence between the two HRSs [28].

Our total systematic uncertainty is evaluated assuming that all uncertainties are un-correlated. [24]. The uncertainties of the acceptance cuts were obtained varying individual cuts according to their corresponding resolution. The uncertainties on the target position were obtained

varying the target position in the MC. We also studies the effect of the optics on our event selection, using various sets of the optical matrix obtained varying the dipole and quadrupole magnetic fields of the HRS magnets. [24, 28].

We set our E_m ranges as 0-30 MeV, 30-54 MeV, and 54-90 MeV. We integrated the missing energy distribution for each of the ranges and performed the fit on the corresponding missing momentum distribution to improve our sensitivity.

We performed a χ^2 minimization using the missing energy and missing momentum distributions as function of the spectroscopic factors, mean value and width of each of the ^{48}Ti orbitals.

We used 100 bins (1 MeV) for the missing energy and 40 bins for the missing momentum with different range in momentum depending upon the kinematics. The reduced MC cross section [44] and the ratio of the data to simulation yield was determined using:

$$\frac{d^2\sigma^{\rm red}_{cc1}}{d\Omega dE'} = \left(\frac{d^2\sigma^{\rm red}_{cc1}}{d\Omega dE'}\right)_{\rm MC} \times \frac{Y(E',\theta)}{Y_{\rm MC}(E',\theta)}. \tag{3.5}$$

$Y(E',\theta)$ is the yield for a given bin in missing energy or missing momenta. The reduced MC cross section is a parametrization obtained using existing data [46] and includes the following:

1. the σ_{cc1} cross section of de Forest [42],
2. the spectral function factorization,
3. the radiative corrections according to the model of Mo and Tsai [47],
4. the Coulomb corrections as in Ref. [48],
5. the FSI corrections

Eq. 3.5 utilizes the ratio of the experimentally-detected and theoretically-simulated electron yield defined as:

$$Y = L \cdot \sigma^{obs} \cdot \Delta E \cdot \Delta\Omega \cdot A$$
$$Y_{MC} = L \cdot \sigma^{MC} \cdot \Delta E \cdot \Delta\Omega \cdot A_{MC}, \tag{3.6}$$

where Y is one way to express the yield that was observed experimentally and Y_{MC} is a Monte Carlo dependent yield base on simulation. In both cases, L is an integrated luminosity, ΔE represents the above mentioned energy bin, and $\Delta\Omega$ represents the angle-proxy for momentum bin. σ^{MC} is shorthand for the Monte Carlo dependent cross section and σ^{obs} is the cross section that can be derived directly from data. A and A_{MC} are respectively the data and MC acceptances, or probabilities that a particle generated in the target can pass through the spectrometer and be measured in the HRSs. A core assumption of the ratio method is that One underline assumption of the method used here, called ratio method, is that the MC reproduces quite accurately the data. A consequence of the ratio method is that it is heavily reliant on simulation and can potentially bias the analysis. However, it has been shown that the ratio method produces a cross section that is in good agreement with a less simulation-reliant method [26], namely the acceptance correction method. Where the acceptance is computed for the data and we do not rely so heavily on the MC simulation.

The next step will be to compare our data against the SF model used as input in the SIMC simulation. As previously stated in Ch. 1, Eq. 1.11 can be factorized in term of the elementary cross-section and the spectral function itself. And the spectral function can further be parameterized following the prescription outlined in Ch. 3.

We can now take our reduced-observed cross section and compare it against the SF prediction using a χ^2 minimization procedure. For this purpose we use a ROOT [49] based fitting

Table 3.5: Results of the χ^2 minimization using the missing momentum distributions, including and excluding the correlated spectral function. N here indicate the occupational number.

		w/ corr.	w/o corr.
α	N_α	S_α	
$1d_{3/2}$	2	0.78 ± 0.05	0.78 ± 0.09
$2s_{1/2}$	2	2.07 ± 0.07	2.10 ± 0.10
$1d_{5/2}$	6	2.27 ± 0.04	2.27 ± 0.08
$1p_{1/2}$	2	2.72 ± 1.23	2.72 ± 0.34
$1p_{3/2}$	4	3.36 ± 0.04	3.53 ± 0.06
$1s_{1/2}$	2	2.54 ± 0.04	2.65 ± 0.02
corr.	0	0.48 ± 0.01	excluded
$\sum_\alpha S_\alpha$		14.48 ± 1.24	14.05 ± 0.38
d.o.f.		1,132	1,133
χ^2/d.o.f.		1.9	3.2

program called MINUIT [50].

The χ^2 function is defined as:

$$\chi^2 = \sum_i \chi_i^2 = \sum_i \left(\frac{\sigma_i^{\text{red, obs}} - \sum_\alpha S_\alpha f_\alpha^{\text{pred}}(i)}{\sigma_{\sigma_i^{\text{red, obs}}}} \right)^2, \tag{3.7}$$

where the index i labels the missing momentum bin, α is the orbital index, $f_\alpha^{\text{pred}}(i)$ is the parametrized prediction evaluated at bin i in the missing momentum spectra for orbital α, S_α is the spectroscopic factor, $\sigma_\sigma$are the uncertainties.

The missing momentum distribution, as in the case of the Ar, does not show dependence on the mean energies and widths of the orbitals.

Table 3.5 provides a summary of the fit of the missing momentum distributions including the degrees of freedom and the value of the χ^2. The fit was repeated excluding the correlated part of the SF to avoid possible bias.

Table 3.6: χ^2 minimization external constraints coming from Ref. [51, 52, 53, 54].

Parameter	Value (MeV)	Uncertainty (MeV)
$E(1d_{3/2})$	12.529	0.002
$E(2s_{1/2})$	12.925	0.002
$E(1d_{5/2})$	18.229	0.015
$E(1p_{3/2}) - E(1p_{1/2})$	4.1	1.5

Table 3.7: Results of the χ^2 minimization using the missing energy distributions using different set of priors, with and without the correlated part of the SF.

		all priors	w/o p_m	w/o corr.
α	N_α		S_α	
$1d_{3/2}$	2	0.89 ± 0.11	1.42 ± 0.20	0.95 ± 0.11
$2s_{1/2}$	2	1.72 ± 0.15	1.22 ± 0.12	1.80 ± 0.16
$1d_{5/2}$	6	3.52 ± 0.26	3.83 ± 0.30	3.89 ± 0.30
$1p_{1/2}$	2	1.53 ± 0.21	2.01 ± 0.22	1.83 ± 0.21
$1p_{3/2}$	4	3.07 ± 0.05	2.23 ± 0.12	3.12 ± 0.05
$1s_{1/2}$	2	2.51 ± 0.05	2.05 ± 0.23	2.52 ± 0.05
corr.	0	3.77 ± 0.28	3.85 ± 0.25	excluded
$\sum_\alpha S_\alpha$		17.02 ± 0.48	16.61 ± 0.57	14.12 ± 0.42
d.o.f		206	231	232
χ^2/d.o.f.		1.9	1.4	2.0

We then repeat the fit minimizing the χ^2 function using the missing energy spectra,

$$\chi^2 = \sum_i \chi_i^2 + \sum_n \left(\frac{\tau_n^{\text{fit}} - \tau_n^c}{\sigma_n^{\text{fit}}} \right)^2 . \tag{3.8}$$

where τ_n^{fit} is a particular fit parameters and the τ_n^{c} is the external constraint and the σ_n^{fit} is the error on the fit parameters.

We include additional constraints (summarized in Table 3.6) in the form of penalty terms to the χ^2 function using data from Ref. [51, 52, 53, 54].

The spin-orbit splitting has been computed using the phenomenological prescription of

Table 3.8: Results of the minimization of the χ^2 over the missing energy distributions. Also here we included or exclude the correlated part of the Sf from the fit.

	E_α (MeV)		σ_α (MeV)	
α	w/ priors	w/o priors	w/ priors	w/o priors
$1d_{3/2}$	12.53 ± 0.02	10.90 ± 0.12	1.9 ± 0.4	1.6 ± 0.4
$2s_{1/2}$	12.92 ± 0.02	12.57 ± 0.38	3.8 ± 0.8	3.0 ± 1.8
$1d_{5/2}$	18.23 ± 0.02	17.77 ± 0.80	9.2 ± 0.9	9.6 ± 1.3
$1p_{1/2}$	28.8 ± 0.7	28.7 ± 0.7	12.1 ± 1.0	12.0 ± 3.6
$1p_{3/2}$	33.0 ± 0.3	33.0 ± 0.3	9.3 ± 0.5	9.3 ± 0.5
$1s_{1/2}$	53.4 ± 1.1	53.4 ± 1.0	28.3 ± 2.2	28.1 ± 2.3
corr.	24.1 ± 2.7	24.1 ± 1.7	—	—

Ref. [53, 54], We had 20 parameters total in the χ^2 minimization using the missing energy spectra. We used spectroscopic factor, the position of the maximum, and the width of the distribution for each of the orbitals and the strength and the threshold energy for the correlate part of the SF. The detailed results are shown in Table 3.7.

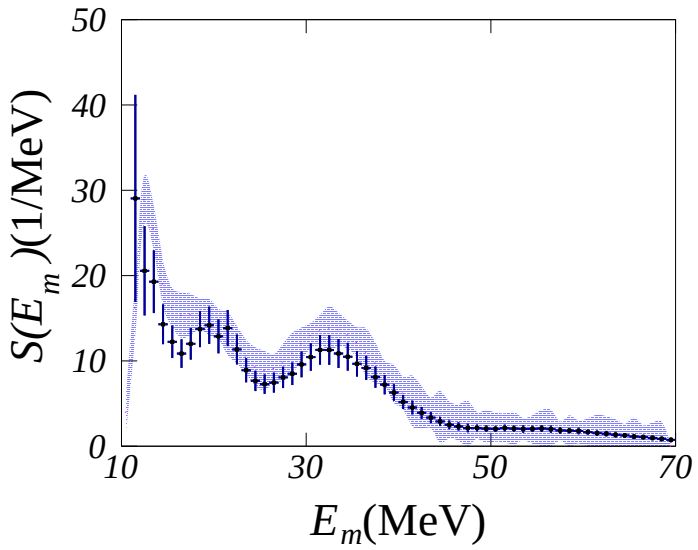

Figure 3.3: Example of the missing energy distributions for argon with p_m range between 140 and 210 MeV/c. The blue band is the fit results with the complete uncertainties [24].

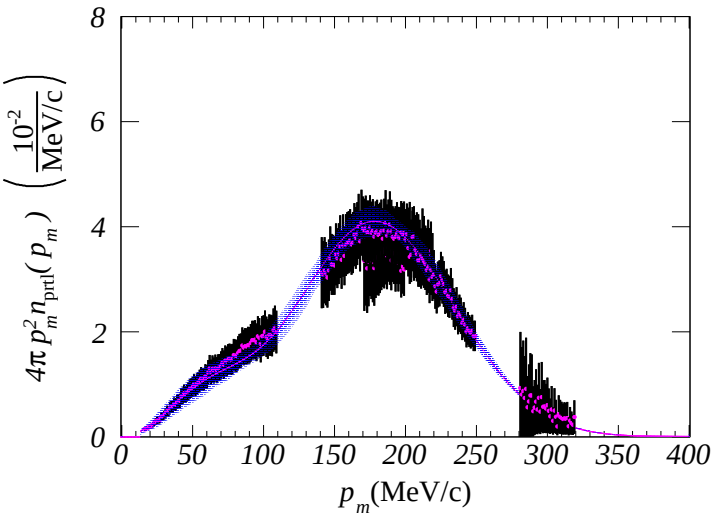

Figure 3.4: Momentum distribution integrated over missing energy between 0 and 30 MeV. Data is presented for all experimental kinematics [24].

As in our previous publications [24] we have evaluated the effects of different priors used in the fit including orbital modeling and parametrization and we found that the results are compatible within uncertainties.

Fig. 3.3 shows that the test spectral function model, rescaled using the parameters obtained from the fit, listed in Table 4.5, is capable of reproducing our data satisfactorily.

Figure 3.4 reports the missing momentum distribution obtained after integrating the data and the model over the missing energy range 30–54 MeV. It is apparent that the collected data cover the relevant kinematic range with just a few exceptions, most notably at vanishing p_m. The experimental coverage is not complete due to experimental conditions and beam-time limitations. In particular, data for kinematics 4 is statistically limited.

Fig. 3.4 shows a good agreement—within uncertainties—of the reduced cross sections using data from kinematics 2 and 3. As observed in Ref. [24], this agreement supports, in Ti as in Ar, the validity of the factorisation scheme used in computing the DWIA corrections.

Chapter 4

Determination of the titanium spectral function from $(e, e'p)$ data

The work described in this chapter was contributed by: L. Jiang, et al. (The Jefferson Lab Hall A Collaboration). It has been published on Physical Review D as:

L. Jiang, et al. (The Jefferson Lab Hall A Collaboration), "Determination of the titanium spectral function from (e, e′p) data" [40].

I have contributed part of the data analysis work in this paper under Professor Mariani's supervision. I worked mainly on the χ^2 minimization procedure and parametrization of the Spectral Functions in the fit. I have compared different fit results and evaluated how different priors and constraints affected the final results, including the dependence of the results from the correlated part of the Spectral Function.

Introduction: The recent measurement of the ${}^{40}_{18}\mathrm{Ar}(e, e'p)$ cross section—performed by the E12-14-012 collaboration in Jefferson Lab Hall A—has enabled the first determination of the spectral function describing the joint energy-momentum distribution of protons in the target nucleus [24].

The JLab experiment, while also providing valuable new information on single-nucleon dynamics in complex nuclei, was primarily meant to obtain the input needed to improve the interpretation of data collected by neutrino experiments using liquid argon detectors, thus

reducing the systematic uncertainty of neutrino energy reconstruction.

In principle, the extension of the analysis based on nuclear spectral functions to both neutrino and antineutrino interactions would require the availability of the neutron energy-momentum distribution in argon, whose experimental study using electron beams involves challenging issues.

The analysis of the data collected by a pioneering $^4\mathrm{He}(e, e'n)$ experiment, carried out at NIKHEF in the 1990s [55], has clearly demonstrated that—in contrast to the case of the $(e, e'p)$ reaction—neutron knockout involves additional difficulties, associated with both the detection of the outgoing neutron and a reliable identification of the reaction mechanism. A comparison between the results of theoretical calculations and the measured cross section, corresponding to momentum transfer $q = 250$ MeV/c and missing momentum in the range $25 < p_{\mathrm{miss}} < 70$ MeV/c, shows that in this kinematic regime charge-exchange processes—in which the detected neutron is *not* produced at the elementary interaction vertex—provide the dominant contribution, and must be carefully taken into account.

An alternative, admittedly rather crude, procedure to obtain information on the neutron distribution in argon is based on the observation that the neutron spectrum of $^{40}_{18}\mathrm{Ar}$ is mirrored by the proton spectrum of the nucleus of titanium, having charge $Z = 22$. Based on this property, which reflects the isospin symmetry of nuclear forces, it has been argued that the proton spectral function obtained from $\mathrm{Ti}(e, e'p)$ data provides a viable proxy for the neutron spectral function of argon [25]. The validity of this hypothesis is supported by the results of Ref. [18], whose authors have employed the proton and neutron spectral functions of argon obtained from a state-of-the-art theoretical model to carry out an accurate calculation of the double-differential $^{40}_{18}\mathrm{Ar}(\nu_\mu, \mu^-)$ cross section. The results obtained replacing the neutron spectral function of argon with the proton spectral function of titanium turn out to be in remarkably good agreement; in fact, they are nearly indistinguishable from one

another.

In the following, we report the results of the analysis of the Ti$(e, e'p)$ data collected in Jefferson Lab Hall A by the E12-14-012 collaboration, and discuss the representation of the reduced cross sections in terms of a model proton spectral function.

Experimental setup: Experiment E12-14-012 was approved by the Jefferson Lab PAC in 2014 and data was taken in the Spring 2017. In the past few years a series of measurements have been completed: the inclusive, (e, e') [25, 26, 27], and exclusive $(e, e'p)$ [24, 28] electron scattering cross sections on several targets, including a natural gas argon target [24, 28].

An electron beam of 2.2 GeV and $\approx$ 22 μA was provided by the Jefferson Lab Continuous Electron Beam Accelerator Facility (CEBAF). The scattered protons and electrons were detected in coincidence in two nearly identical high-resolution spectrometers (HRSs) both consisting of a dipole and three quadrupole magnets. The electron and proton spectrometers are both equipped with vertical drift chambers (VDCs) [39], scintillator planes (two) for timing measurements and triggering, and a double-layered lead-glass calorimeter. In addition, the electron arm is equipped with a gas Čerenkov counter for particle identification and pion rejectors, while the proton arm is equipped with pre-shower and shower detectors [33]. The experimental kinematics used during data taking on the natural titanium target were identical for kinematic 2-4 to those used for the Ar target [24] and in the case of kinematic 1 the missing energy was set to 50 MeV.

We determine the six-fold differential cross section as a function of p_m and E_m following the same method as described in Ref. [24]. The reduced cross section was obtained as a function of p_m and E_m, from the double differential cross section using the elementary electron-proton off-shell cross section σ_{ep} of de Forest [42, 43]. The simulated momentum distributions are presented in Fig. 4.1. The missing energy of the shell-model states is assumed to follow the

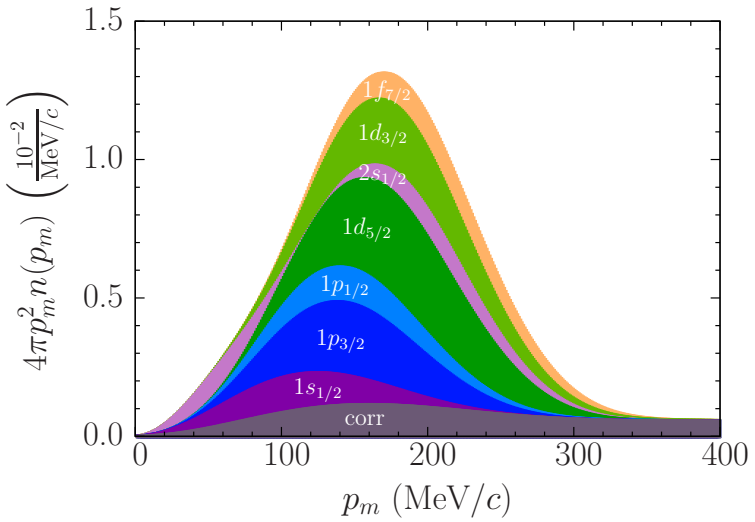

Figure 4.1: Missing momentum distribution of protons in titanium in the test spectral function, presented with the geometric factor of $4\pi p_m^2$.

Gaussian distribution as in Ref. [24], with the peak positions determined as described in detail elsewhere [28].

The JLab SIMC spectrometer package [46] was used to simulate $(e, e'p)$ events including an approximate spectral function for Ti, geometric details of the target, radiative corrections, and Coulomb effects.

The correlated spectral function is estimated within the approach of Ref. [56], as a convolution integral involving the momentum distributions of the relative and center-of-mass motion of a correlated proton-neutron pair [24]. By construction, the correlated part accounts for 20% of the total strength of the test spectral function, see Table 4.1. Compared with the correlated spectral function of argon, the one for titanium differs due to different mass number A, and the employed value of the pn knockout threshold. These differences translate into a higher absolute number of correlated pn pairs in titanium than in argon, and slightly different energy of the residual system. On the other hand, the parameters of the relative motion of the pn pairs and their center-of-mass motion are assumed not to differ between argon and titanium.

Table 4.1: Parametrization of the test spectral function of protons in titanium. The missing energy distribution of a shell-model state α peaked at E_α has width σ_α, and is normalized to the spectroscopic factor S_α. For comparison, we also show the occupation number in the independent particle shell-model N_α. For the correlated part, we provide the total normalization and the threshold for two-nucleon knockout $E_{\rm thr}$.

α	N_α	S_α	E_α (MeV)	σ_α (MeV)
$1f_{7/2}$	2	1.6	11.45	2
$1d_{3/2}$	4	3.2	12.21	2
$2s_{1/2}$	2	1.6	12.84	2
$1d_{5/2}$	6	4.8	15.46	4
$1p_{1/2}$	2	1.6	35.0	6
$1p_{3/2}$	4	3.2	40.0	6
$1s_{1/2}$	2	1.6	62.0	10
corr.	—	4.4	22.09	—

Figure 4.2 displays the test spectral function as a function of missing momentum and missing energy.

We observe an energy resolution for the Ti states comparable to the one of the Ar target, this is due mainly to the FSI corrections in our MC simulation that contribute to a broadening of the states.

Data Analysis: The total systematic uncertainty in this analysis is the sum in quadrature of the individual uncertainties as listed in Table 4.2. We followed the same procedure as described in Ref. [24]: kinematic and acceptance cuts are considered uncorrelated bin to bin and they do not depend on the theoretical input model. All the kinematic and acceptance cuts were varied according to the variable's resolution. The simulation did not contain **a** correction for final state interaction (FSI) effects other than the transparency corrections.

We repeated the analysis of systematic uncertainties varying all MC input parameters, and the effect on the analysis was found to be negligible. To determine the uncertainties related to the target position, we varied the simulation's inputs within uncertainties, and we used a

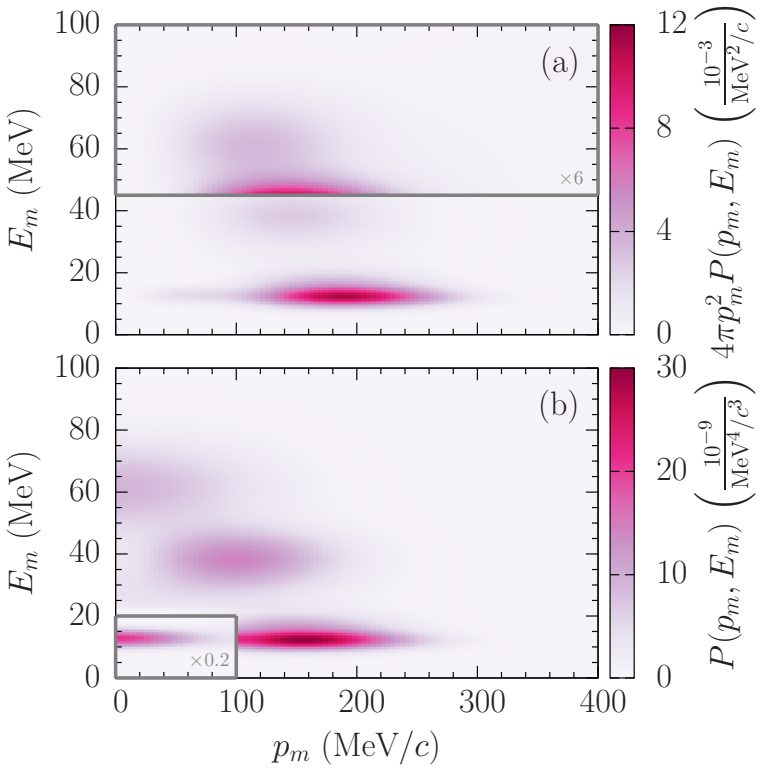

Figure 4.2: Test spectral function shown (a) with and (b) without the geometric factor of $4\pi p_m^2$. Note that multiplicative factors are used for clearer presentation of some regions.

Table 4.2: Contributions to systematic uncertainties for titanium averaged over all the E_m and p_m bins for each kinematics. All numbers are in %. For kin4, the results correspond to the systematic uncertainties of the signal and the background added in quadrature.

	kin1	kin2	kin3	kin4
1. Total statistical uncertainty	0.78	0.60	0.82	1.24
2. Total systematic uncertainty	4.63	4.92	4.70	6.04
a. Beam x&y and HRS offset	0.75	1.71	1.19	1.47
b. Optics (q1, q2, q3)	0.48	0.77	0.55	0.90
c. Acceptance cut (θ, ϕ, z)	1.36	1.46	1.32	1.57
d. Target thickness/density/length	0.20	0.20	0.20	0.20
e. Calorimeter & Čerenkov & β cuts	0.29	0.58	0.42	2.83
f. Radiative and Coulomb corr.	1.00	1.00	1.00	1.00
g. Cross section model and FSI	4.12	2.23	2.23	2.23
h. Trigger and coincidence time cut	0.78	0.33	0.58	2.32

different optical transport matrix obtained using independent variation of each of the three quadrupole magnetic fields. For each of this variation we computed the effect with respect to a run where no variations were used and the differences were summed in quadrature. The total systematic uncertainty is then computed using the same assumptions and recipe as described in Ref. [24, 28].

We set our E_m ranges, 0 to 30 MeV, 30 to 54 MeV, and 54 to 90 MeV. We then integrated the missing energy distribution for each of the ranges and performed the fit on the corresponding missing momentum distribution to improve our sensitivity.

We fit the experimental missing energy and missing momentum distributions to extract spectroscopic factors, mean value and width of each of the ^{48}Ti orbitals.

For each bin in the spectra of missing energy (100 $\times$ 1 MeV) and missing momentum (40 bins with different range in momentum depending upon the kinematics), we computed the reduced MC cross section [44] and the ratio of the data to simulation yield, and we combined them as the following:

$$\frac{d^2\sigma^{\rm red}_{cc1}}{d\Omega dE'} = \left(\frac{d^2\sigma^{\rm red}_{cc1}}{d\Omega dE'}\right)_{\rm MC} \times \frac{Y(E',\theta)}{Y_{\rm MC}(E',\theta)}, \tag{4.1}$$

where the $Y(E',\theta)$ is the yield for a given bin and the reduced MC cross section is a fit to the existing data [46]. The reduced cross section includes (i) the σ_{cc1} cross section of de Forest [42], (ii) the predictions of the spectral function model, (iii) radiative corrections [47], (iv) Coulomb corrections [48], and (v) FSI corrections, described within the distorted-wave impulse approximation (DWIA) scheme.

The fit performs a χ^2 minimization using the MINUIT [50] package available in ROOT [49].

The χ^2 function is defined as:

$$\chi^2 = \sum_i \chi_i^2 = \sum_i \left(\frac{\sigma_i^{\text{red, obs}} - \sum_\alpha S_\alpha f_\alpha^{\text{pred}}(i)}{\sigma_{\sigma_i^{\text{red, obs}}}} \right)^2, \tag{4.2}$$

where the index i labels the missing momentum bin, α is the orbital index, $f_\alpha^{\text{pred}}(i)$ is the parametrized prediction evaluated at bin i in the missing momentum spectra for orbital α, S_α is the spectroscopic factor. The missing momentum distribution, as in the case of the Ar [24] does not show dependence on the mean energies and widths of the orbitals.

Table 4.3 provides a summary of the fit of the missing momentum distributions including the degrees of freedom and the value of the χ^2. The fit was repeated excluding the correlated part of the SF to avoid possible bias.

The spectroscopic factors reported in Tables 4.3 and 4.5 are normalized to $80\% \times 22$ for the total strength of the orbitals and to $20\% \times 22$ for the correlated part and they include corrections due to phase space coverage.

We then repeat the fit minimizing the χ^2 function using the missing energy spectra,

$$\chi^2 = \sum_i \chi_i^2 + \sum_n \left(\frac{\tau_n^{\text{fit}} - \tau_n^c}{\sigma_n^{\text{fit}}} \right)^2. \tag{4.3}$$

We include additional constraints (summarized in Tab. 4.4) in the form of penalty terms to the χ^2 function using data from Ref. [51, 52, 53, 54].

The spin-orbit splitting has been computed using the phenomenological prescription of Ref. [53, 54], $E(n,l,l-1/2) - E(n,l,l+1/2) = \frac{2l+1}{2n} k A^{-C}$, with angular momentum l, main quantum number n, and mass number A. The empirically determined constants $k = 23.27$ MeV and $C = 0.583$ [53] are included in the fit as penalty function to the χ^2. The uncertainty value has been calculated comparing the prediction of the phenomenological prescription to the available experimental data from NIKHEF-K [57, 58, 59]. The fit

Table 4.3: Comparison of the results of the χ^2 minimization using the missing momentum distributions, determined with and without the use of the correlated spectral function. For every state α, we determined the spectroscopic factor S_α, and its occupation number in an independent-particle shell model, N_α. We include the total spectroscopic strength, the number of degrees of freedom (d.o.f.), and the χ^2 per d.o.f.

		w/ corr.	w/o corr.
α	N_α	S_α	
$1f_{7/2}$	2	0.83 ± 1.17	0.78 ± 1.35
$1d_{3/2}$	4	1.17 ± 0.22	1.34 ± 0.10
$2s_{1/2}$	2	2.02 ± 0.08	2.18 ± 0.08
$1d_{5/2}$	6	2.34 ± 1.34	2.34 ± 3.72
$1p_{1/2}$	2	2.46 ± 0.27	2.71 ± 1.19
$1p_{3/2}$	4	5.46 ± 1.69	5.46 ± 0.05
$1s_{1/2}$	2	2.17 ± 0.09	2.51 ± 0.08
corr.	0	5.15 ± 0.41	excluded
$\sum_\alpha S_\alpha$		21.60 ± 2.51	17.32 ± 4.20
d.o.f.		675	676
χ^2/d.o.f.		0.49	0.57

on the missing energy spectra contains 23 parameters: 3 parameters for each orbital (the spectroscopic factor, the position of the maximum, and the width of the distribution) and 2 parameters for the correlated SF (the strength and the threshold energy).

We present our results in Table 4.5. We repeated the fit excluding the results coming from the p_m minimization and without the correlated SF part. All the results are compatible within errors, which indicates no large bias in the determination of the spectroscopic factors using a different set of constraints.

As in our previous publications [24] we have evaluated the effects of different priors used in the fit including orbital modeling and parametrization and we found that the results are compatible within uncertainties.

Fig. 4.3 shows that the test spectral function model, rescaled using the parameters obtained from the fit, listed in Table 4.5, is capable of reproducing our data satisfactorily.

Table 4.4: External constraints on the fits to the missing-energy spectra computed using data from past measurements [51, 52, 53, 54]. For the clarity of presentation, we denote E_α as $E(\alpha)$.

Parameter	Value (MeV)	Uncertainty (MeV)
$E(1f_{7/2})$	11.32	0.10
$E(1d_{3/2})$	12.30	0.24
$E(2s_{1/2})$	12.77	0.25
$E(1d_{5/2})$	15.86	0.20
$E(1d_{5/2}) - E(1d_{3/2})$	3.57	0.31
$E(1p_{3/2}) - E(1p_{1/2})$	6.36	0.75

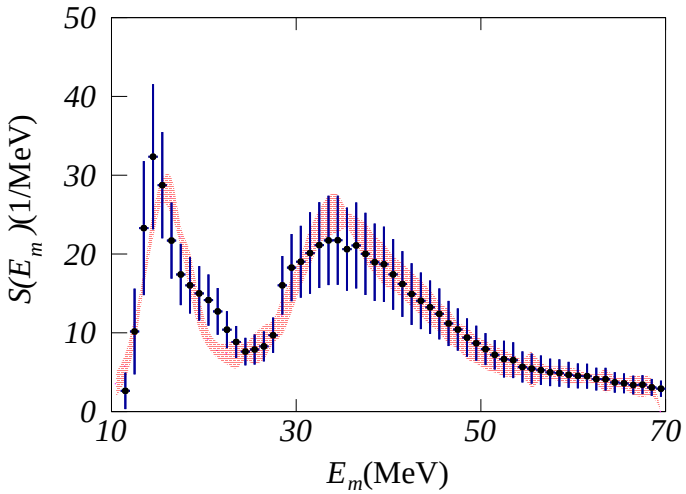

Figure 4.3: Missing energy distributions obtained for natural titanium for $130 < p_m < 260$ MeV/c. The red band indicates the final fit results including the full error uncertainties.

Figure 4.4 reports the missing momentum distribution obtained after integrating the data and the model over the missing energy range 10–30 MeV.

It is apparent that the collected data cover the relevant kinematic range with just a few exceptions, most notably at vanishing p_m. The experimental coverage is not complete due to experimental conditions and beam-time limitations. In particular, data for kinematics 4 is statistically limited.

Table 4.5: Results of the χ^2 minimization using the missing energy distributions for different cases. We repeated the fit with different priors, and not including the correlated part of the SF. For every state α, we extract spectroscopic factor S_α, occupational number N_α assuming independent particle model and total spectroscopic strength. We reported at the end also the number of degrees of freedom (d.o.f.), and the χ^2 per d.o.f.

		all priors	w/o p_m	w/o corr.
α	N_α		S_α	
$1f_{7/2}$	2	1.53 ± 0.25	1.55 ± 0.28	1.24 ± 0.22
$1d_{3/2}$	4	2.79 ± 0.37	3.15 ± 0.54	3.21 ± 0.37
$2s_{1/2}$	2	2.00 ± 0.11	1.78 ± 0.46	2.03 ± 0.11
$1d_{5/2}$	6	2.25 ± 0.16	2.34 ± 0.19	3.57 ± 0.29
$1p_{1/2}$	2	2.00 ± 0.20	1.80 ± 0.27	2.09 ± 0.19
$1p_{3/2}$	4	2.90 ± 0.20	2.92 ± 0.20	4.07 ± 0.15
$1s_{1/2}$	2	2.14 ± 0.10	2.56 ± 0.30	2.14 ± 0.11
corr.	0	4.71 ± 0.31	4.21 ± 0.46	excluded
$\sum_\alpha S_\alpha$		20.32 ± 0.65	20.30 ± 1.03	18.33 ± 0.59
d.o.f		121	153	125
χ^2/d.o.f.		0.95	0.71	1.23

Table 4.6: Measured peak positions E_α, widths σ_α, and the parameter $E_{\rm corr}$ of the correlated spectral function obtained from the fit of the missing energy distributions. Results are obtained including and excluding the results from the previous fit performed using the missing momentum.

	E_α (MeV)		σ_α (MeV)	
α	w/ priors	w/o priors	w/ priors	w/o priors
$1f_{7/2}$	11.32 ± 0.10	11.31 ± 0.10	8.00 ± 5.57	8.00 ± 6.50
$1d_{3/2}$	12.30 ± 0.24	12.33 ± 0.24	7.00 ± 0.61	7.00 ± 3.84
$2s_{1/2}$	12.77 ± 0.25	12.76 ± 0.25	7.00 ± 3.76	7.00 ± 3.84
$1d_{5/2}$	15.86 ± 0.20	15.91 ± 0.22	2.17 ± 0.27	2.23 ± 0.29
$1p_{1/2}$	33.33 ± 0.60	33.15 ± 0.65	3.17 ± 0.45	3.03 ± 0.48
$1p_{3/2}$	39.69 ± 0.62	39.43 ± 0.68	5.52 ± 0.70	5.59 ± 0.70
$1s_{1/2}$	53.84 ± 1.86	52.00 ± 3.13	11.63 ± 1.90	13.63 ± 2.59
corr.	25.20 ± 0.02	25.00 ± 0.29	—	—

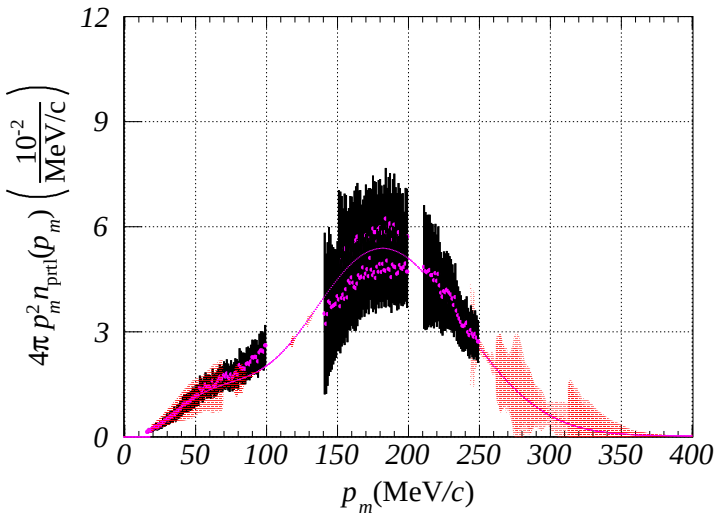

Figure 4.4: Partial momentum distribution obtained by integrating the test spectral function over the missing energy range of 10–30 MeV presented with the geometric factor of $4\pi p_m^2$. Different data regions represent data from different kinematics.

Fig. 4.4 shows a good agreement—within uncertainties—of the reduced cross sections using data from kinematics 2 and 3. As observed in Ref. [24], this agreement supports, in Ti as in Ar, the validity of the factorisation scheme used in computing the DWIA corrections.

Summary and conclusions: The Ti$(e, e'p)$ data collected by experiment E12-14-012 at Jefferson Lab have been analysed to extract the proton spectral function in Ti. The spectral function, an innate property of the nucleus, provides the energy and momentum distribution of protons bound in the titanium ground state. Our spectral function derivation depends only from the model used to compute FSI corrections. The FSI uncertainties have been evaluated in the same way as in Ref. [24, 28] and have been included in our measurements.

The results of our study of titanium provide important new and much needed information, and it will play a critical to further develop theoretical models capable of describing neutrino-nucleus interactions in liquid argon detectors like DUNE.

The results of the pioneering work of Barbieri *et al.* [18] that uses one of our previous

results [25, 26, 27] demonstrate the importance of the availability of electron scattering data in Ar and Ti. The work in Ref. [18] showed that a replacement of the neutron SF of argon with the proton SF of $^{48}_{22}$Ti in the calculation of the $^{40}_{18}\mathrm{Ar}(\nu_\mu, \mu^-)$ cross section at beam energy $E_\nu = 1$ GeV has a few-percent effect. It has to be kept in mind, however, that the inclusive cross section, which only involves integrals of the SFs, is rather insensitive to the details of the missing energy distributions. Therefore, the findings of Barbieri *et al.*, while being very encouraging, cannot be taken as clear-cut evidence of the validity of the assumption that the proton SF of natural titanium can be used as a proxy for the neutron SF of Ar, as suggested by isospin symmetry. More work will be necessary to put this hypothesis on a firm basis. Here we only note that our estimate of the top four energy levels of neutrons in $^{40}_{18}$Ar suggests that they agree to 0.6–2.2 MeV with those of protons in $^{48}_{22}$Ti listed in Tab. 4.1.

The reduced differential cross sections has been fitted using a model spectral function. The effects of FSI, which are known to be significant in $(e, e'p)$ reactions, have been included using the same factorization scheme which underlines our analysis and, as for the case of Ar [24], seems to be reliable.

The comparison between data and MC simulation results has been shown in a broad range of missing energies, extending from the proton-knockout threshold to $E_m \sim 80$ MeV. The overall agreement supports the validity of the theoretical basis of our analysis.

We have determined the position and width of the peaks corresponding to shell model states, and estimated the corresponding spectroscopic strengths.

A more accurate determination of the titanium spectral function will require a more advanced theoretical model of the energy and momentum distributions, as well as a refined implementation of the DWIA.

The extraction of the spectral function reported in this article—providing a satisfactory de-

scription of the proton energy and momentum distribution—should be seen as the achievement of the goals of the JLab experiment E12-14-012, and a step toward a more accurate description of (anti)neutrino interactions in argon.

The understanding of the proton and neutron spectral functions for argon will greatly improve the accuracy of neutrino and antineutrino energy reconstruction in measurements of neutrino oscillations, such as those in the short-baseline program of Fermilab and in the long-baseline studies in the Deep Underground Neutrino Experiment.

As a final remark it should be pointed out that, up to FSI corrections, the factorisation ansatz—whose validity is clearly demonstrated by the observation of y-scaling [60]—provides the basis for the extraction of the spectral function from $(e, e'p)$ data. The spectral function can be employed to describe initial state physics in any processes in which the beam particle couples to a single nucleon, including quasi elastic scattering, resonance production and deep inelastic scattering [61]. In correlated systems, these processes lead to the appearance of both 1p1h and 2p2h final states. On the other hand, the description of 2p2h final states originating from coupling to the two-nucleon meson-exchange currents requires an extension of the factorisation scheme, and the use of two-nucleon spectral functions, as discussed in Ref. [62].

Chapter 5

Concluding Remarks

The purpose of this thesis was to analyze the data collected in 2017 by the JLab Experiment E12-14-012. The published paper [40], reported in Ch. 4 highlights years of work done by the Hall A Collaboration leading to the fulfillment of E12-014-12's goal: produce the first data set of its kind - a description of the proton and neutron energy-momentum distributions in Argon [1].

The experiment was motivated by the needs of precision modeling of neutrino-nucleus interactions as explained in Ch. 1, where furthermore we explain why this investigation of nuclear theory is critical in particular to ensure the success of the DUNE [4] experiment. The (e,e′p) reactions were used to determine the spectral function of proton and neutron in argon. In Ch. 2 the layout of JLab's Hall A and the experimental detectors and conditions were detailed to describe the journey that the electrons and protons took. How such data comes together by requiring a vast array of measurements built on the backs of decades of trusted scientific principles. Ch. 3 introduces the underlying process that is required to perform the analysis by looking at the measurements of Ar(e,e′p). Namely it is necessary to understand the theory in order to model/build an adequate simulation and to extract meaningful data. These two necessary items come together in statistical χ^2 analysis to inform us if our understanding of nuclear theory has merit. As with any model or assertion though, this is not to say that anything is proven. It is simply a step towards refining our understanding of Ti and Ar through rigorous testing. Future studies are now needed, as the

data passes onto the next wave of scientists, who will continue working, refining and testing models. For example, future nuclear theorists can look back on E12-14-012 as a necessary step to probing the assumptions that led to uniting Ti and Ar data and if the scheme can be extended into more complicated final states. Future neutrino experimentalists can take these precise measurements as an appropriate refinement in the understanding of a major target medium and further test the models discussed here with increasing scrutiny and required precision when reconstructing a notoriously difficult particle.

Bibliography

[1] O. Benhar *et al.*, Measurement of the Spectral Function of ^{40}Ar through the (e,e'p) reaction, arXiv:1406.4080 [nucl-ex] (2014)

[2] Krishanu Majumdar and Konstantinos Mavrokoridis, Review of Liquid Argon Detector Technologies in the Neutrino Sector, arXiv:2103.06395v1 [physics.ins-det] (2021)

[3] Huber, J., and Jepsen, K. (2015). The dawn of DUNE. Symmetry Magazine.

[4] DUNE Collaboration, The DUNE Far Detector Interim Design Report Volume 1: Physics, Technology and Strategies, arXiv:1807.10334 [physics.ins-det]

[5] 19-0078-02.hr.jpg Retrieved March 23, 2023, from https://mod.fnal.gov/mod/stillphotos/2019/0000/19-0078-02.hr.jpg

[6] LBNE Collaboration, The Long-Baseline Neutrino Experiment: Exploring Fundamental Symmetries of the Universe, arXiv:1307.7335 [hep-ex]

[7] L. Alvarez-Ruso *et al.*, NuSTEC White Paper: Status and Challenges of Neutrino-Nucleus Scattering arXiv:1706.03621v2 [hep-ph] (2017)

[8] O. Benhar and A. Fabrocini and S. Fantoni, Nucl. Phys. A, 267, The Nucleon Spectral Function in Nuclear Matter, 505, 1989, doi:10.1016/0375-9474(89)90374-6

[9] S. Boffi, C. Giusti and F.D. Pacati, (1982). Structure functions in quasi-free (e,e'p) reactions. Nuclear Physics A, 386(3), 599–616. doi:10.1016/0375-9474(82)90039-2

[10] Thomas, A.W. and Weise, W. (2001) The Structure of the Nucleon. Wiley-VCH, Berlin. http://dx.doi.org/10.1002/352760314X

[11] M. Riou, Information on Nuclear Strucure from $(p, 2p)$ and other Knock-Out Reactions, Rev. Mod. Phys., 37, 3, 375-387, (Jul, 1965), doi:10.1103/RevModPhys.37.375

[12] Jan Ryckebusch, Wim Cosyn, and Maarten Vanhalst, What densities can be effectively probed in quasifree single-nucleon knockout reactions?, arXiv:1102.0905v1 [nucl-th] (2011)

[13] J.J. Kelly, *et al.*, Density dependence in the two-nucleon effective interaction at 135 MeV. Phys Rev C Nucl Phys. 1989 Apr;39(4):1222-1241. doi: 10.1103/physrevc.39.1222. PMID: 9955328.

[14] Tsoulfanidis, N., and Landsberger, S. (2010). Measurement and detection of radiation. CRC Press LLC.

[15] Matthias Burkardt, James J. Kelly, J.W. Negele (Ed.), Erich Vogt (Ed.), (2002). Advances in Nuclear Physics Volume 23. Kluwer Academic Publishers

[16] pers. comm. C. Mariani

[17] A. Misiejuk *et al.*, Electron-Induced Neutron Knockout from ^{4}He, Phys. Rev. Lett., 89, 17, 172501, 4, (Oct 2002), doi:10.1103/PhysRevLett.89.172501

[18] C. Barbieri, N. Rocco, and V. Somà, Phys. Rev. C **100**, 062501 (2019).

[19] P. Bączyk *et al.*, (2018). Isospin-symmetry breaking in masses of N Z nuclei. Physics Letters B, 778, 178–183. doi:10.1016/j.physletb.2017.12.068

[20] Dominique Marchand. Calcul des corrections radiatives à la diffusion compton virtuelle. Mesure absolue de l'énergie du faisceau d'électrons de Jefferson Lab. (Hall A) par une méthode magnétique : projet ARC. Physique Nucléaire Théorique [nucl-th]. Université Blaise Pascal - Clermont-Ferrand II, 1998. Français. ffNNT : ff. fftel-00298382f

[21] S. Frullani and J. Mougey, Adv. Nucl. Phys. **14**, 1 (1984).

[22] C. Giusti and F.D. Pacati, Phys. Rev. C **67**, 044601 (2003).

[23] S. Boffi, C. Giusti, F. Pacati, and S. Frullani, Nucl. Phys. **A319**, 461 (1979).

[24] L. Jiang *et al.* (Jefferson Lab Hall A Collaboration), Phys. Rev. D **105**, 112002 (2022).

[25] H. Dai, *et al.* (Jefferson Lab Hall A Collaboration), Phys. Rev. C **98**, 014617 (2018).

[26] H. Dai *et al.* (Jefferson Lab Hall A Collaboration), Phys. Rev. C **99**, 054608 (2019).

[27] M. Murphy *et al.* (Jefferson Lab Hall A Collaboration), Phys. Rev. C **100**, 054606 (2019).

[28] L. Gu *et al.* (Jefferson Lab Hall A Collaboration), Phys. Rev. C **103**, 034604 (2021).

[29] J. P. Chen, Spin Structure of the Nucleon, Hirschegg Workshop, 2004

[30] J. Berthot and P. Vernin (1999) Beam Energy Measurement in Hall-A of CEBAF, Nuclear Physics News, 9:4, 12-16, DOI: 10.1080/10506899909411146

[31] J.-C. Denard *et al.*, HIGH ACCURACY BEAM CURRENT MONITOR SYSTEM FOR CEBAF'S EXPERIMENT HALL A, Proceedings of the 2001 Particle Accelerator Conference, Chicago

[32] Jay Benesch and Yves Roblin (2021) Redesigning the Jefferson Lab Hall A Beam Line for High Precision Parity Experiments

[33] J. Alcorn *et al.*, Nucl. Instrum. Methods Phys. Res. A **522**, 294 (2004).

[34] S. N. Santiesteban et al., Nucl. Instrum. Methods Phys. Res. A 940, 351 (2019)

[35] I. Rodriquez, and D.W. Higinbotham. (2008). "REVIVING AND UPGRADING OF THE EP DEVICE". United States. https://www.osti.gov/servlets/purl/1052103.

[36] J. L. Herraiz, doi:10.2172/1056354

[37] C. Hyde-Wright *et. al* Beam Position Studies for E93050 (1999)

[38] 2017 Version: Jefferson Lab Hall A Standard Equipment Manual The Hall A Collaboration Editor: D.W. Higinbotham and T. Keppel 2019

[39] K. G. Fissum *et al.*, Nucl. Instrum. Methods Phys. Res. A **474**, 108 (2001).

[40] L. Jiang *et al.* [Jefferson Lab Hall A], Phys. Rev. D **107**, no.1, 012005 (2023) doi:10.1103/PhysRevD.107.012005 [arXiv:2209.14108 [nucl-ex]].

[41] T. Nikšić, N. Paar, D. Vretenar, and P. Ring, Comput. Phys. Commun. 185, 1808 (2014).

[42] T. de Forest Jr., Nucl. Phys. A **392**, 232 (1983).

[43] A. E. L. Dieperink, T. de Forest Jr., I. Sick, and R. A. Brandenburg, Phys. Lett. B **63**, 261 (1976).

[44] J. Arrington *et al.*, Phys. Rev. Lett. **82**, 2056 (1999).

[45] L. Frankfurt, M. Strikman and M. Zhalov, Phys. Lett. B **503**, 73-80 (2001) doi:10.1016/S0370-2693(01)00173-3 [arXiv:hep-ph/0011088 [hep-ph]].

[46] SIMC Monte Carlo, https://hallcweb.jlab.org/wiki/index.php/SIMC_Monte_Carlo.

[47] L. W. Mo and Y. S. Tsai, Rev. Mod. Phys. **41**, 205 (1969).

[48] A. Aste, C. von Arx, and D. Trautmann, Eur. Phys. J. A **26**, 167 (2005).

[49] R. Brun and F. Rademakers, Nucl. Instrum Methods Phys. Res. A **389**, 81 (1997).

[50] F. James, "MINUIT Function Minimization and Error Analysis: Reference Manual Version 94.1," CERN-D-506.

[51] Meng Wang, G. Audi, F. G. Kondev, W. J. Huang, S. Naimi, and Xing Xu, Chin. Phys. C **41**, 030003 (2017).

[52] J. Chen, Nucl. Data Sheets **149**, 1 (2018).

[53] G. Mairle, M. Seeger, H. Reinhardt, T. Kihm, K. T. Knöpfle, and Chen Lin Wen, Nucl. Phys. A **565**, 543 (1993).

[54] G. Mairle, Phys. Lett. B **304**, 39 (1993).

[55] A. Misiejuk *et al.*, Phys. Rev. Lett. **89**, 172501 (2002).

[56] C. Ciofi degli Atti and S. Simula, Phys. Rev. C **53**, 1689 (1996).

[57] G. J. Kramer *et al.*, Phys. Lett. B **227**, 199 (1989).

[58] M. Leuschner *et al.*, Phys. Rev. C **49**, 955 (1994).

[59] G. J. Kramer, The proton spectral function of ^{40}Ca and ^{48}Ca studied with the $(e, e'p)$ reaction. An investigation of ground-state correlations, Ph.D. thesis, University of Amsterdam, 1990.

[60] I. Sick, D. Day and J. S. Mccarthy, Phys. Rev. Lett. **45**, 871-874 (1980) doi:10.1103/PhysRevLett.45.871

[61] E. Vagnoni, O. Benhar, and D. Meloni, Phys. Rev. Lett. **118**, 142502 (2017).

[62] O. Benhar, A. Lovato and N. Rocco, Phys. Rev. C **92**, no.2, 024602 (2015) doi:10.1103/PhysRevC.92.024602 [arXiv:1502.00887 [nucl-th]].